THE CLUSTER ION SPECTROMETRY (CIS) EXPERIMENT

H. RÈME, J. M. BOSQUED, J. A. SAUVAUD, A. CROS, J. DANDOURAS,
C. AOUSTIN, J. BOUYSSOU, Th. CAMUS, J. CUVILO, C. MARTZ, J. L. MÉDALE,
H. PERRIER, D. ROMEFORT, J. ROUZAUD and C. d'USTON
CESR, BP 4346, 31028 Toulouse Cédex 4, France

E. MÖBIUS, K. CROCKER, M. GRANOFF, L. M. KISTLER and M. POPECKI
UNH, Durham, U.S.A.

D. HOVESTADT, B. KLECKER, G. PASCHMANN and M. SCHOLER
MPE, Garching, Germany

C. W. CARLSON, D. W. CURTIS, R. P. LIN and J. P. McFADDEN
SSL, Berkeley, U.S.A.

V. FORMISANO, E. AMATA, M. B. BAVASSANO-CATTANEO, P. BALDETTI,
G. BELLUCI, R. BRUNO, G. CHIONCHIO and A. DI LELLIS
IFSI, Frascati, Italy

E. G. SHELLEY, A. G. GHIELMETTI and W. LENNARTSSON
Lockheed, Palo Alto, U.S.A.

A. KORTH and H. ROSENBAUER
MPAE, Lindau, Germany

R. LUNDIN and S. OLSEN
SISP, Kiruna, Sweden

G. K. PARKS and M. McCARTHY
U.W., Seattle, U.S.A.

H. BALSIGER
Bern University, Bern, Switzerland

Abstract. The Cluster Ion Spectrometry (CIS) experiment is a comprehensive ionic plasma spectrometry package on-board the four Cluster spacecraft capable of obtaining full three-dimensional ion distributions with good time resolution (one spacecraft spin) with mass per charge composition determination. The requirements to cover the scientific objectives cannot be met with a single instrument. The CIS package therefore consists of two different instruments, a Hot Ion Analyser (HIA) and a time-of-flight ion COmposition and DIstribution Function analyser (CODIF), plus a sophisticated dual-processor-based instrument-control and Data-Processing System (DPS), which permits extensive on-board data-processing. Both analysers use symmetric optics resulting in continuous, uniform, and well-characterised phase space coverage. CODIF measures the distributions of the major ions (H^+, He^+, He^{++}, and O^+) with energies from $\sim$0 to 40 keV/e with medium (22.5°) angular resolution and two different sensitivities. HIA does not offer mass resolution but, also having two different sensitivities, increases the dynamic range, and has an angular resolution capability (5.6° × 5.6°) adequate for ion-beam and solar-wind measurements.

Space Science Reviews **79:** 303–350, 1997.

1. Scientific Objectives and Experiment Capabilities

The prime scientific objective of CIS is the study of the dynamics of magnetised plasma structures in the vicinity of the Earth's magnetosphere, with emphasis on the physics of the Earth's bow shock, the magnetopause boundary, the polar cusp, the geomagnetic tail and the plasma sheet. Past experience has demonstrated that the study of the macrophysics and microphysics requires that the local orientation and the state of motion of the plasma structures be determined as accurately as possible. The four Cluster spacecraft with relative separation distances that can be adjusted to spatial scales of the structures (a few hundred kilometers to several thousand kilometers) give for the first time the unambiguous possibility to distinguish spatial from temporal variations. These scientific objectives require the investigation of many different phenomena, including solar-wind/magnetopause interactions, substorms and auroras, reconnection, generation of field-aligned currents, polar cusps and upstream foreshock dynamics.

The Cluster spacecraft will encounter ionic plasma of vastly diverse characteristics in the course of one year (Figure 1). A highly versatile and reliable ionic plasma experiment is therefore needed.

The variety of conditions encountered in the various magnetospheric regions sets a number of requirements in order to provide scientifically valuable products everywhere.

(1) A great dynamic range is necessary in order to detect fluxes as low as those of the lobes, but also those as high as solar-wind fluxes, throughout the solar cycle.

(2) Hot populations are present in vast regions of the magnetosphere and of the magneto-sheath. In order to provide a satisfactory and uniform coverage of the phase space with sufficient resolution, a broad energy range and a full 4π angular coverage are necessary. The angular resolution should be sufficient to be able to separate multiple populations, such as gyrating or transmitted ions from the main population downstream of the bow shock, and to be able to detect fine structures in the distributions.

(3) Cold beams, such as the solar wind, require a high angular and energy resolution in a limited energy and angular range. Because of the limited energy range required, a beam tracking algorithm should be implemented in order to be able to follow the beam in velocity space. Moreover, for example in the foreshock regions, any study of backstreaming ions requires the simultaneous observation of the solar-wind cold beam and of the backstreaming particles. Therefore, together with the solar-wind coverage described above, a coverage of the entire phase space excepting the sunward sector, with broad energy range, is also required.

(4) In the case of sharp boundaries, such as discontinuities or boundary crossings, it is necessary not to miss any information at the discontinuity, thus a very efficient means of mode change, which allows adaptation to the local plasma conditions, should be provided.

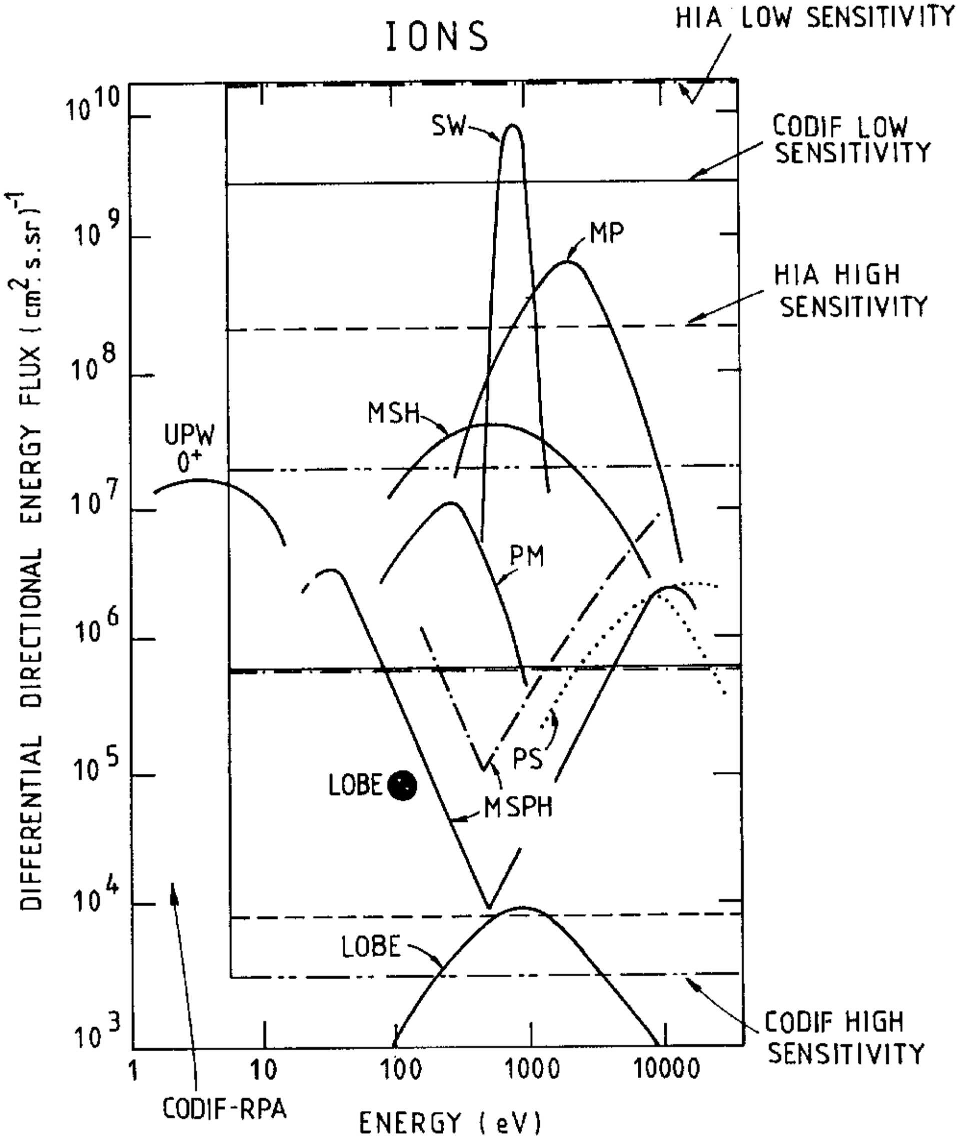

Figure 1. Representative ion differential directional energy fluxes to be encountered in the solar wind (SW), the magnetopause (MP), the magnetosheath (MSH), the plasma mantle (PM), the magnetosphere (MSPH), the plasma sheet (PS), the lobe and upwelling ions (UPW). The range studied by the low sensitivity of HIA is limited by - · - · - · - · - · - · - · - · -, the range of the high sensitivity of HIA by -, the range of low sensitivity of CODIF by full lines, and the range of high sensitivity of CODIF by - ·· - ·· - ·· - ·· - ·· - ·· - ··.

(5) Moments of the whole three-dimensional (3D) distribution (and of the sunward sector, in solar-wind mode) should be computed on-board , with high time

resolution, to continuously generate key parameters, necessary for event identification.

(6) To study detailed phenomena of magnetospheric plasma physics all the particle populations must be identified and characterized, therefore a 3D distribution is needed. In order to transmit the full 3D distribution, while overcoming the telemetry rate limitations, a compression algorithm must be introduced, which allows an increased amount of information to be transmitted.

So, to meet the scientific objectives, the CIS instrumentation has been designed to satisfy the following criteria, simultaneously on the 4 spacecraft:

– Provide uniform coverage for ions over the entire 4π steradian solid angle with good angular resolution.

– Separate the major mass ion species, i.e., those which contribute significantly to the total mass density of the plasma (generally H^+, He^{++}, He^+, and O^+).

– Have high sensitivity and large dynamic range ($\geq 10^7$) to support high-time-resolution measurements over the wide range of plasma conditions to be encountered in the Cluster mission (Figure 1).

– Have high ($5.6^\circ \times 5.6^\circ$) and flexible angular sampling resolution to support measurements of ion beams and solar wind.

– Have the ability to routinely generate on-board the fundamental plasma parameters for major ion species and with one spacecraft spin time resolution (4 s). These parameters include the density (n), velocity vector ($\mathbf{V}$), pressure tensor (P), and heat flux vector ($\mathbf{H}$).

– Cover a wide range of energies, from spacecraft potential to 40 keV e^{-1}.

– Have versatile and easily programmable operating modes and data-processing routines to optimize the data collection for specific scientific studies and widely varying plasma regimes.

– Rely as much as possible on well-proven sensor designs flown successfully on the AMPTE and *Giotto* missions.

To satisfy all these criteria, the CIS package consists of two different instruments: a Hot Ion Analyser (HIA) sensor and a time-of-flight ion COmposition and DIstribution Function (CODIF) sensor.

The CIS plasma package is versatile and is capable of measuring both the cold and hot ions of Maxwellian and non-Maxwellian populations (for example, beams) from the solar wind, the magnetosheath, and the magnetosphere (including the ionosphere) with sufficient angular, energy and mass resolutions to meet the scientific objectives. The time resolution of the instrument is sufficiently high to follow density or flux oscillations at the gyrofrequency of H^+ ions in a magnetic field of 10 nT or less. Such field strengths will be frequently encountered by the Cluster mission. Oscillations of O^+ at the gyrofrequency can be resolved outside 6–7 R_E. So this instrument package will provide all of the ionic plasma data required to meet the Cluster science objectives (Escoubet and Schmidt, 1997).

Cluster has been conceived as a global instrument which allows, using four spacecraft, vorticity, gradients, divergences, ... to be determined and thus enables macroscopic quantities, for example the electric current from the Curl-B to be measured. Electric currents perpendicular to the magnetic field can also been determined from the pressure gradient of particles. In the simplest case of an ideal magneto-hydromagnetic equilibrium, the perpendicular current density can be written $J_\perp = (B \times \nabla P)/B^2$. More details about the ∇P method accuracy can be found in Martz (1993) and in Martz and Sauvaud (1995). For a satellite distance which is small compared to the current filament transverse dimensions, the ∇P method gives good results. The Curl-B method can give less accurate results due to errors on the magnetic field and the satellite separation. On the contrary for a satellite distance which is comparable to the current filament dimensions, the mathematical error introduced by the non-linear variations of the pressure drives an error which becomes very large when a satellite is located outside the current filament. The Curl-B method is free of this latter error. Thus the Curl-B method and the pressure-gradient methods are complementary for estimating the electric currents.

With its capability to provide three-dimensional distribution functions simultaneously for several major species with high time resolution, the CIS instrument will make substantial contributions to the study of the solar-wind magnetosphere interaction, the dynamics of the magnetosphere, the physics of the magnetopause boundary, the polar cusp and the plasma sheet boundary layer, the upstream foreshock and solar-wind dynamics, the magnetic reconnection and the field-aligned current phenomena. For example an important contribution will be made to the understanding of the formation of the bow shock and its role in the heating and acceleration of incoming ion populations, to take just an example.

At the quasi-perpendicular bow shock the specular reflection of ions, their subsequent energy gain in the upstream $\mathbf{V}_{\mathrm{sw}} \times \mathbf{B}$ convection electric field, and their final escape into the downstream region, are known to be important in the dissipation of energy at the shock. The scale length on which the scattering of the original ring distribution and the final thermalisation occurs can at best be guessed (Sckopke *et al.*, 1990). With separation distances from a few 100 km to a few 1000 km the vital scales of several ion gyro radii can be covered with the spacecraft configuration. In addition, CIS will provide the ion distribution functions separately for all major species with a time resolution of one spacecraft spin. Therefore, it will be possible to study the behaviour of He^{++} at the shock. Because of their higher energy all He^{++} ions penetrate the shock. Their bulk velocity is larger than that of the protons, and the entire He^{++} population therefore gyrates in the downstream region. This difference is particularly important. Although the He^{++} ions make up only $\sim$ 6% of the solar wind density, their contribution to the heating downstream of the shock must be comparable to that of the few percent of protons which are reflected and then start to gyrate. Finally, He^{+} pick-up ions of interstellar origin in the solar wind (Möbius *et al.*, 1985, 1988; Gloeckler *et al.*, 1993) present another important source for ion reflection and downstream heating and thermalization. Because pick-up ions fill a sphere in velocity space with a radius equal to the solar wind speed, centred around the solar wind, ions will interact differently with the shock depending on their origin in velocity space. CIS will provide the resolution to determine the original pick-up distribution and the fate of the reflected ions.

The quasi-parallel bow shock is known to be the source of a diffuse energetic ion population and low-frequency waves. The recent success with hybrid simulations has demonstrated that the energetic ion and wave activity are necessary ingredients of the shock formation which itself is a high dynamic (or even quasi-cyclic) process (e.g., Quest, 1988; Burgess, 1989; Scholer and Terasawa, 1990). This simulation work has paved the way for a combined in-depth study of the evolution of the ion distributions across the shock and their temporal variation with the CIS instrument. As has been shown in a modelling with simulated spacecraft (Giacalone *et al.*, 1994), a close collaboration between the data analysis and simulations will be needed for this task. It can also be expected that the association of ion density enhancements with magnetic pulses upstream of the shock can be identified with CIS and the multi-spacecraft capabilities (Scholer, 1995) as opposed to statistical studies which only yield an average spatial distribution (Trattner *et al.*, 1994). These new measurements will significantly further our understanding of the wave-particle interactions at the bow shock and their importance for ion acceleration and shock structure.

2. The Hot Ion Analyser (HIA)

The Hot Ion Analyser (HIA) instrument combines the selection of incoming ions according to the ion energy per charge ratio by electrostatic deflection in a symmetrical quadrispherical analyser which has a uniform angle-energy response with a fast imaging particle detection system. This particle imaging is based on microchannel plate (MCP) electron multipliers and position encoding discrete anodes.

2.1. Electrostatic Analyser Description

Basically the analyser design is a symmetrical quadrispherical electrostatic analyser which has a uniform 360° disc-shaped field of view (FOV) and extremely narrow angular resolution capability. This symmetric quadrisphere or 'top hat' geometry (Carlson *et al.*, 1982) has been successfully used on numerous sounding rocket flights as well as on the AMPTE/IRM, Giotto and WIND spacecraft (Paschmann *et al.*, 1985; Rème *et al.*, 1987; Lin *et al.*, 1995).

The operating principles of the analyser are illustrated by cross-section and top views in Figure 2. The symmetric quadrisphere consists of three concentric spherical elements. These three elements are an inner hemisphere, an outer hemisphere which contains a circular opening, and a small circular top cap which defines the entrance aperture. This analyser is classified as quadrispherical simply because the particles are deflected through 90°. In either analyser a potential is applied between

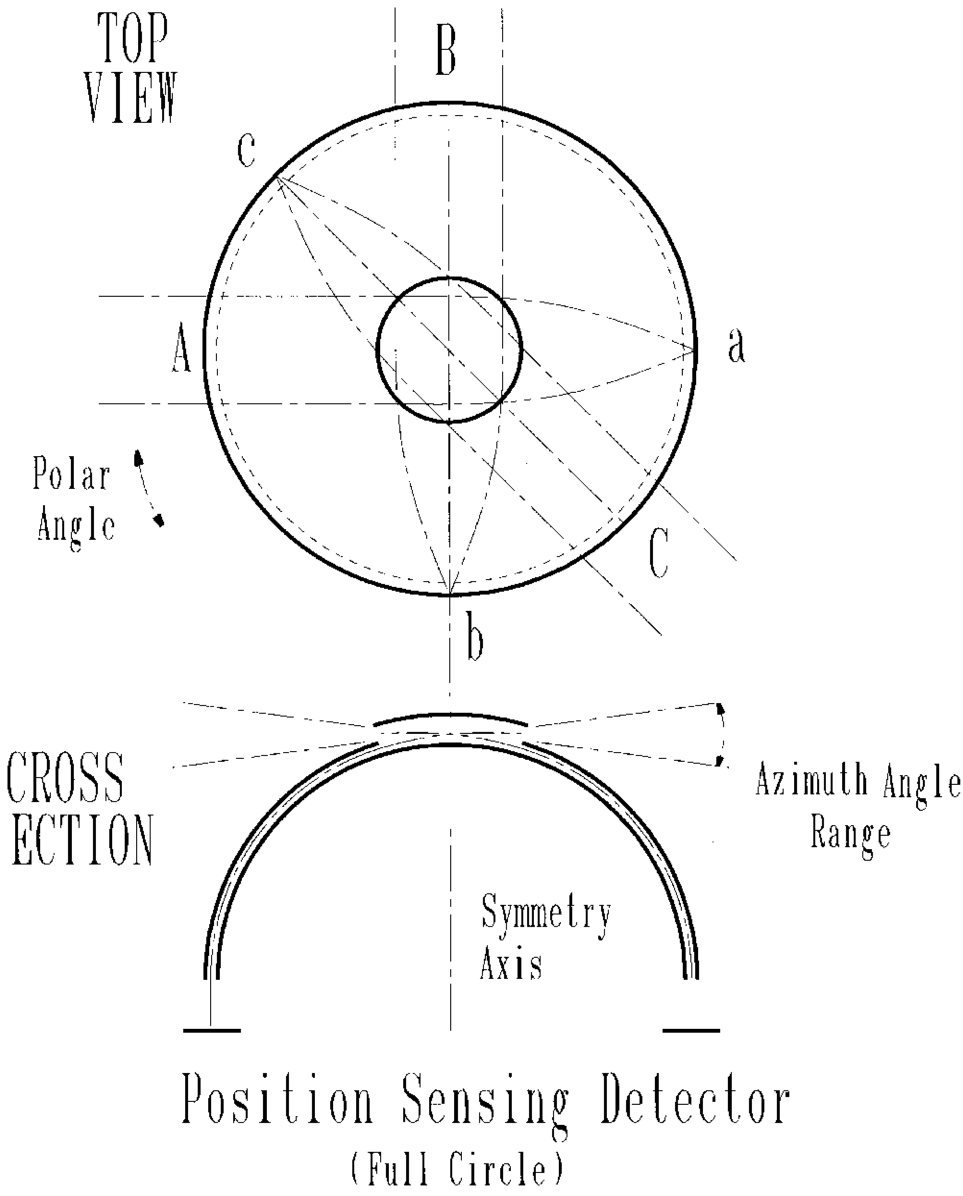

Figure 2. Particle orbits in a normal quadrisphere and in a symmetrical quadrisphere.

the inner and outer plates and only charged particles with a limited range of energy and initial azimuth angle are transmitted. The particle exit position is a measure of the incident polar angle which can be resolved by a suitable position-sensitive detector system. The symmetric quadrisphere makes the entire analyser, including the entrance aperture, rotationally symmetric. Trajectories are shown to illustrate

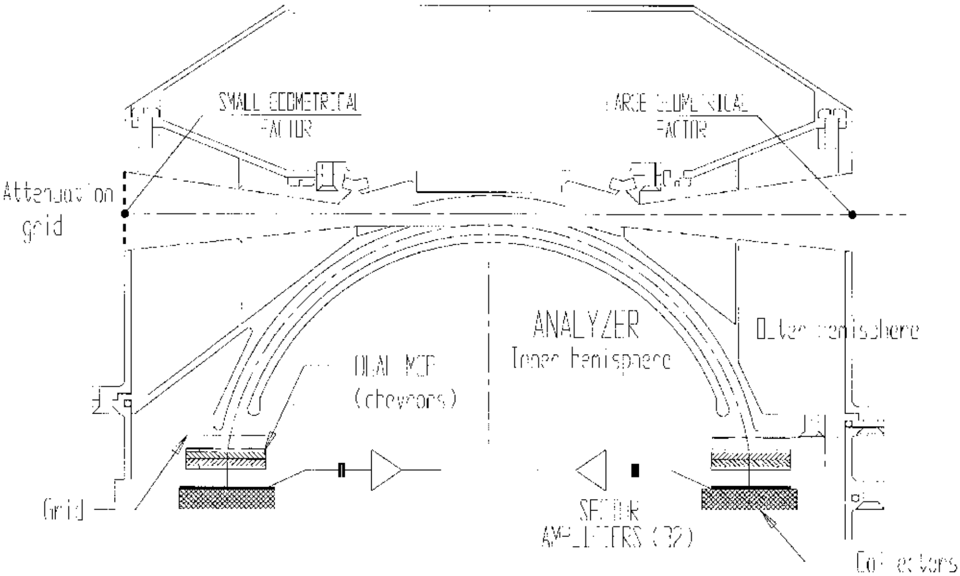

Figure 3. Principle of the HIA electrostatic analyser.

the focusing characteristics which are independent of polar angle. Throughout the paper we will use the following convention: the angle about the spin axis is the azimuth angle whereas the angle out of the spin plane is called polar angle.

In conclusion the symmetrical quadrispherical analyser has good focusing properties, sufficient energy resolution, and the large geometrical factor of a quadrisphere. Because of symmetry, it does not have the deficiencies of the conventional quadrisphere, namely limited polar angle range and severely distorted response characteristics at large polar angles, and it has an uniform polar response.

The HIA instrument has $2 \times 180°$ FOV sections parallel to the spin axis with two different sensitivities, with a ratio 20–30 (depending of the flight model and precisely known from calibrations), corresponding respectively to the 'high G' and 'low g' sections. The 'low g' section allows detection of the solar wind and the required high angular resolution is achieved through the use of $8 \times 5.625°$ central anodes, the remaining 8 sectors having in principle 11.25° resolution; the 180° 'high G' section is divided into 16 anodes, 11.25° each. In reality, sectoring angles are respectively $\sim$ 5.1° and $\sim$ 9.7°, as demonstrated by calibrations (see Section 2.5). This configuration provides 'instantaneous' 2D distributions sampled once per 62.5 ms ($\frac{1}{64}$ of one spin, i.e., 5.625° in azimuth, which is the nominal sweep rate of the high voltage applied to the inner plate of the electrostatic analyser to select the energy of the transmitted particles. For each sensitivity section a full 4π steradian scan is completed every spin of the spacecraft, i.e., 4 s, giving a full 3D distribution of ions in the energy range $\sim$ 5 eV e^{-1} to 32 keV e^{-1} (the analyser constant being $\sim$ 6.70).

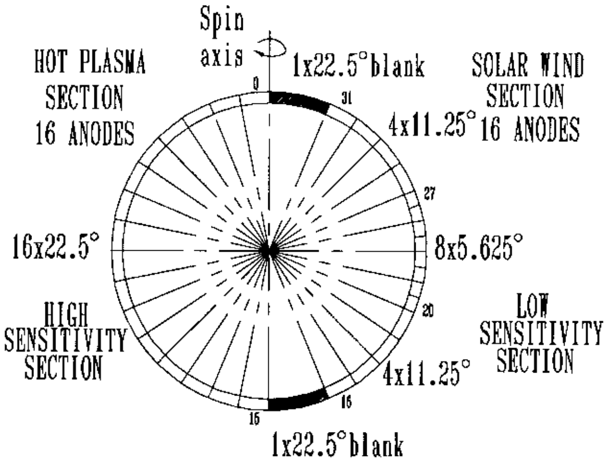

Figure 4. Principle of the HIA anode sectoring.

Figure 3 provides a cross-sectional view of the HIA electrostatic analyser. The inner and outer plate radii are 37.75 mm and 40.20 mm, respectively. The analyser has an entrance aperture which collimates the field of view, defines the two geometrical factors and blocks the solar UV radiation.

2.2. Detection System

A pair of half-ring microchannel plates (MCP) in a chevron pair configuration detects the particles at the exit of the electrostatic analyser. The plates form a $2 \times 180^\circ$ ring shape, each 1 mm thick with an inter-gap of $\sim$ 0.02 mm, with an inner diameter of 75 mm and outer diameter of 85 mm. The MCPs have 12.5 μm straight microchannels with a bias angle of 8° to reduce variations in MCP efficiency with azimuthal direction. The chevron configuration with double thickness plates provides a saturated gain of 2×10^6, with a narrow pulse height distribution. The plates have a high strip current to provide fast counting capability. For a better detection efficiency ions are post-accelerated by a $\sim$ 2300 V potential applied between the front of the first MCP and a high-transparency grid located $\sim$ 1 mm above. The anode collector behind the MCPs is divided into 32 sectors, each connected to its own pulse amplifier (Figure 4).

2.3. Sensor Electronics

Signals from each of the 32 MCP sectors are sent through 32 specially designed very fast A121 charge-sensitive amplifier/discriminators (Figure 5) that are able to count at rates as high as 5 MHz. Output counts from the 32 sectors are accumulated in 48 counters (including 16 redundant counters for the solar wind), thus providing the basic angular resolution matrix according to the resolution of the anode sectoring.

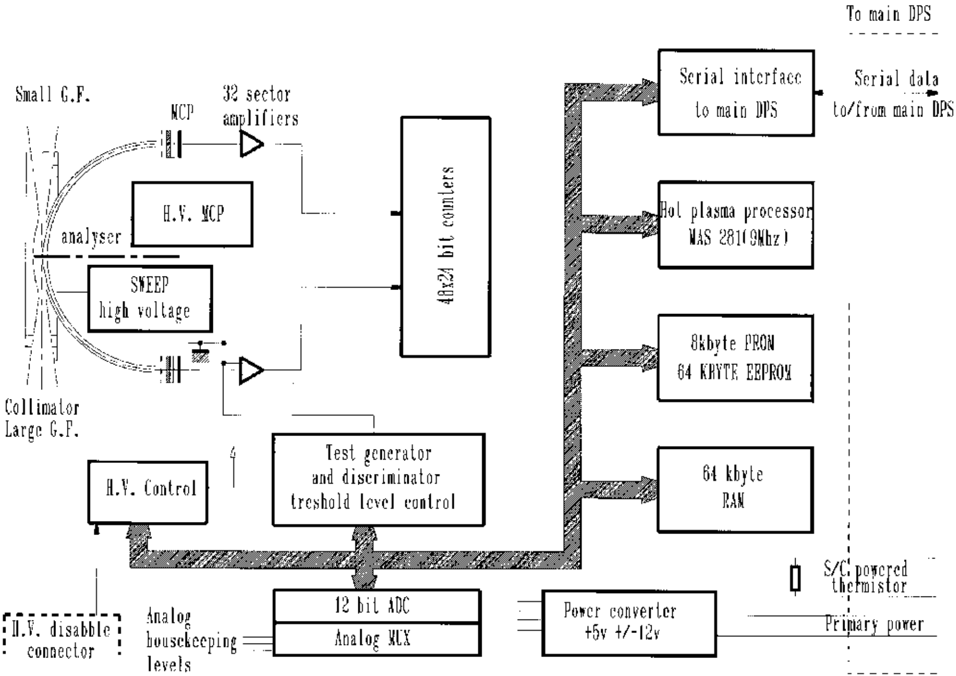

Figure 5. HIA functional block diagram.

According to the operational mode several angular resolutions can be achieved:

– in the normal resolution mode, the full 3D distributions are covered in $\sim 11.2°$ angular bins ('high G' geometrical factor); this is the basic mode inside the magnetosphere;

– in the high-resolution mode the best angular resolution, $\sim 5.6° \times 5.6°$, is achieved within a 45° sector centred on the Sun direction, using the 'low g' geometrical factor section; this mode is dedicated to the detection of the solar wind and near-ecliptic narrow beams.

Low Power Converter

The primary 28 V is delivered through the CODIF/DPS box to the HIA low-voltage power converter which provides +5 V and ±12 V for digital and analog electronics. In order to reduce the power consumption, HV power supplies are directly powered from the primary 28 V with galvanic insulation between the primary ground and the secondary ground.

High Voltage Power Supplies

HIA needs a high-voltage power supply to polarise MCPs at $\sim$ 2300–2500 V and a sweeping high voltage applied on the inner plate of the electrostatic analyser. The high voltages to polarise the MCPs are adjustable under control of the data processor system (DPS) microprocessor.

The energy/charge of the transmitted ions is selected by varying the deflection voltage applied to the inner plate of the electrostatic analyser, between 4800 and 0.7 V. The exponential sweep variation of the deflection voltage is synchronised with the spacecraft spin period. The sweep should consist of many small steps that give effectively a continuous sweep. The counter accumulation time defines the number of energy steps, i.e., 31 or 62 count intervals per sweep. The covered energy range and the sweeping time are controlled by the onboard processor through a 12-bit DAC and a division in two ranges for the sweeping high voltage. So the number of sweeps per spin, the amplitude of each sweep and the sweeping energy range can be adjusted according to the mode of operation (solar wind tracking, beam tracking, etc.). In the basic and nominal mode the sweep of the total energy range is repeated 64 times per spin, i.e., once every 62.5 ms, giving a $\sim$ 5.6° resolution in azimuth resolution.

The HIA block diagram is shown in Figure 5.

2.4. IN-FLIGHT CALIBRATION TEST

A pulse generator can stimulate the 32 amplifiers under processor control. This way all important functions of the HIA instrument and of the associated on-board processing can easily be tested. A special test mode is implemented for health checking of the microprocessor by making ROM checksums and RAM tests. The sweeping high voltage can be tested by measuring the voltage value of each individual step and the MCP gain can be checked by occasionally stepping MCP HV and by adjusting the discrimination level of charge amplifiers.

Performances of the HIA sensor are shown in Table I and in Figure 1. The full sensor is shown in Figure 6.

2.5. HIA PERFORMANCES

Pre-flight and extensive calibrations of all four HIA flight models were performed at the CESR vacuum test facilities in Toulouse, using large and stable ion beams of different ion species and variable energies, detailed studies of MCPs and gain level variations, MCP matching, angular-energy resolution for each sector from a few tens of eV up to 30 keV. Typical performances of the HIA instrument are reproduced in Figure 7. The analyser energy resolution $\Delta E/E$ (FWHM) is $\sim$18%, almost independent of anode sectors and energy; thus the intrinsic HIA velocity resolution is $\sim$9%, only about half of the average solar wind spread value. This is equivalent to an angular resolution of $\sim$ 5° and is thus quite consistent with the angular resolution capabilities of the instrument, i.e., $\sim$ 5.9° (FWHM) in azimuthal angle, as indicated in Figure 7, and $\sim$ 5.6° in polar angle. The polar resolution stays, as expected, almost constant, $\sim$ 9.70°, over the 16 sectors (anodes 0 to 15) constituting the 'high G' section (Figure 8). Anodes 16 to 31 correspond to the 'low g' section and their response transmission is attenuated by a factor of 20–30

Table I
Main-measured parameters

- Full 3D ion distribution functions
- Flux as a function of time, mass and pitch angle
- Moments of the distribution functions: density, bulk velocity, pressure tensor, heat flux vector
- Beams

ANALYSERS	ENERGY RANGE	ENERGY DISTRIBUTION (FWHM)	TIME RESOLUTION 2D ms	TIME RESOLUTION 3D s	MASS RESOLUTION $M/\Delta M$	ANGULAR RESOLUTION	GEOMETRICAL FACTOR (TOTAL)	DYNAMICS $(cm^2\ sec\ sr)^{-1}$
HOT ION ANALYSER HIA	~ 5eV/e - 32 keV/e	18%	62.5	4	-	~ 5.6° x 5.6°	cm^2.sr.kev 3.5×10^{-4} E(keV) for one half 7.10^{-3} E(keV) for the other half	10^4 - 2×10^{10}
ION COMPOSITION AND DISTRIBUTION FUNCTION ANALYSER CODIF	~ 0 - 40 keV/e Mass range 1 - 32 amu	16%	125	4	~ 4 - 7	~ 11.2° x 22.5°	2.16×10^{-3} cm^2 sr for one half 2.3×10^{-5} cm^2 sr for the other half 3.5×10^{-2} cm^2 sr for the RPA	3.10^3 - 3.10^9

ANALYSERS	FULL INSTANTANEOUS FIELD OF VIEW	MASS	POWER (Nominal Operations)
HOT ION ANALYSER HIA	8° x 360°	2.49 kg	3.36 watts
ION COMPOSITION AND DISTRIBUTION FUNCTION ANALYSER CODIF	8° x 360°	8.30 kg (including Data Processing System)	7.28 watts (including DPS)

CIS Total Weight: 10.79 kg without harness
Average CIS total raw power: 10.64 watts

CIS Telemetry: ~ 5.5 kbit/s
Expected total bit number (for the 4 spacecraft): 10^{12} bits

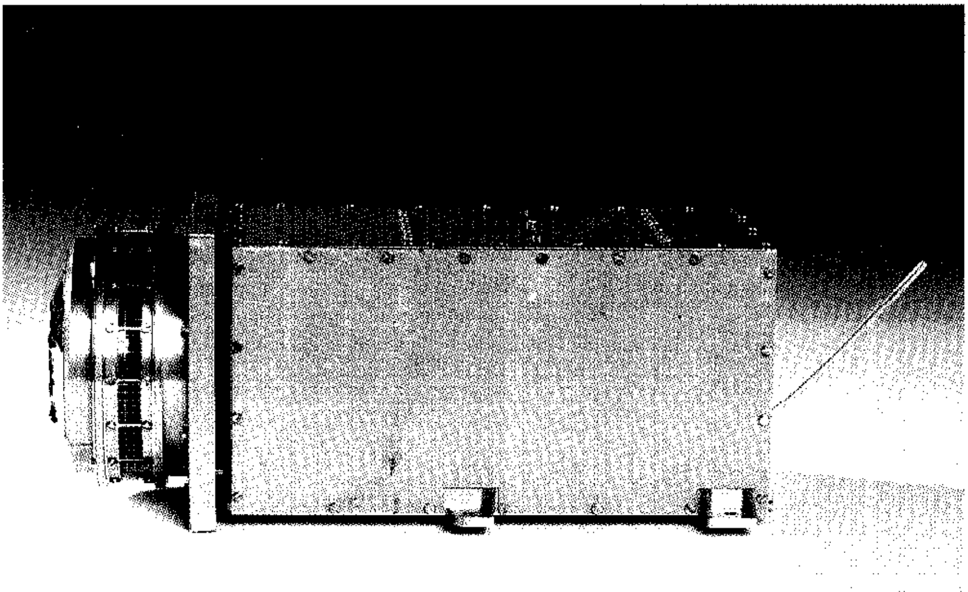

Figure 6. The HIA Sensor.

(depending of the flight model) due to the presence of a pin-hole grid placed in front of the 180° collimator; the polar resolution of sectors 20 to 27 is $\sim$ 5.1°. Thus, when compared to the basic sectoring, $\sim$ 5.6° and $\sim$ 11.2°, all effective polar resolutions are reduced, due to existence of an insulation space between the discrete anodes, as well as by the presence of support posts within the field of view. Finally, experimental energy, angle resolutions and transmission factors are introduced in the geometrical factor used to compute moments of the distribution function.

2.5.1. *UV Rejection*

A number of very interesting events are expected to occur when the HIA spectrometers face the Sun (2 times/spin): of course the intense solar wind, but also, for example, tailward ion beams flowing along the PlasmaSheet Boundary Layer (PSBL). Also a number of measures are applied in order to suppress or limit the solar UV contamination. Part of the UV is rejected by the entrance collimator; moreover, the inner surface of the outer sphere is scalloped and both spheres (and all internal parts) are treated and coated with a special black cupric sulfide. Extensive vacuum chamber tests of the HIA analysers were performed, using a calibrated continuous discharge source for extreme UV at He-584 Å and Lα 1215 Å lines. Reduction of the solar UV light reflectance at the Lα line is demonstrated in Figure 9. The resulting maximum count rate recorded by the sunward looking

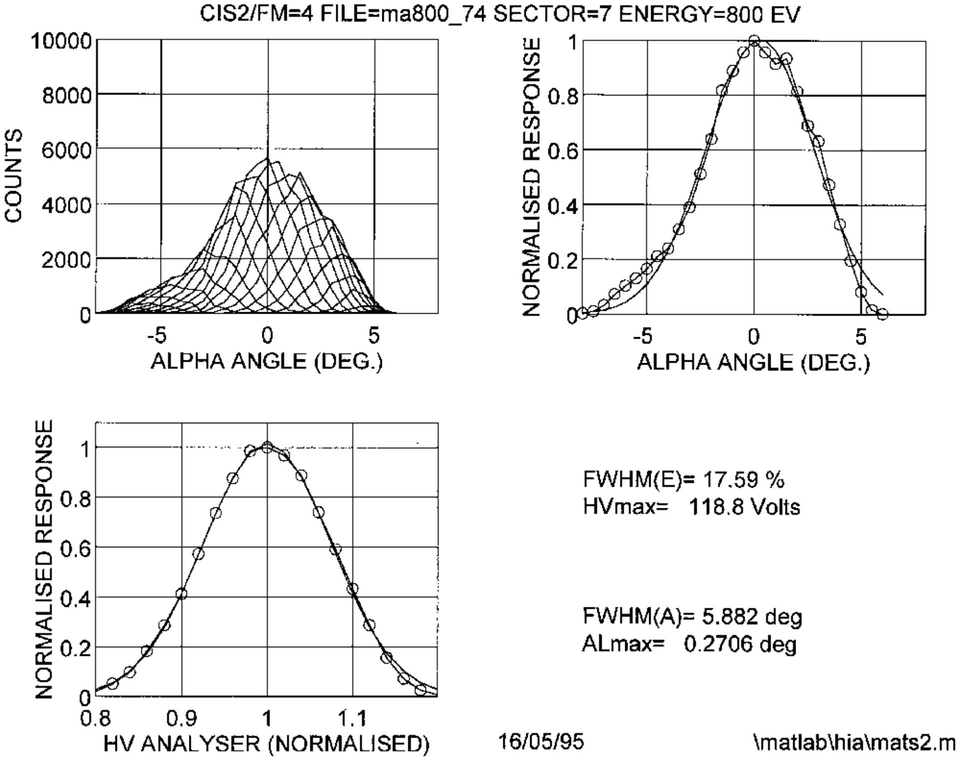

Figure 7. Typical energy and angular resolutions of the HIA analyser (flight model FM4), for an energy beam of 15 keV; the energy resolution is $\sim$ 18% and the intrinsic azimuthal resolution $\sim$ 5.9°.

sector (11.2° wide) is about 80 counts s^{-1} (for an intensity equivalent to 3 Sun intensity units) and the UV contamination is distributed over about $\sim$ 100° in polar angle; such a contamination is acceptable in the solar wind as well as in the magnetosphere.

3. The Ion Composition and Distribution Function Aanalyser (CODIF)

The CODIF instrument is a high-sensitivity mass-resolving spectrometer with an instantaneous 360° $\times$ 8° field of view to measure full 3D distribution functions of the major ion species (as much as they contribute significantly to the total mass density of the plasma), within one spin period of the spacecraft. Typically these include H^+, He^{++}, He^+, and O^+.

The sensor primarily covers the energy range between 0.02 and 40 keV/ charge. With an additional Retarding Potential Analyser (RPA) device in the aperture system of the sensor with pre-acceleration for the energies below 25 eV e^{-1}, the range is extended to energies as low as the spacecraft potential. So, CODIF will cover the core of all plasma distributions of importance of the Cluster mission.

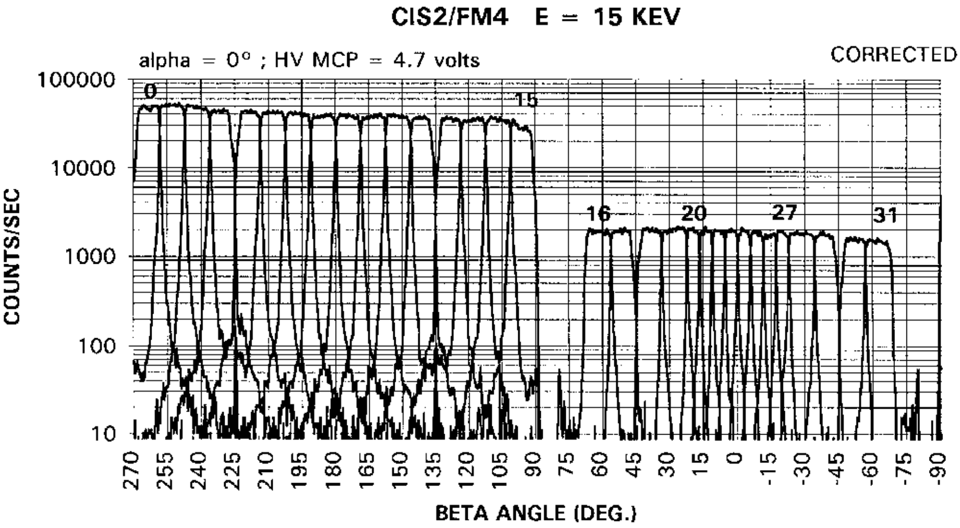

Figure 8. Calibrated relative transmission of the HIA polar sectors (beta angle in the vacuum chamber). Sectors 0–15 have $\sim$ 9.7° (FHWM) angular resolution; transmission of sectors 16–31 is attenuated by a factor of $\sim$ 25 and equatorial sectors 20–27 have $\sim$ 5.1° (FWHM) angular resolution. 0–180° axis corresponds to the spacecraft spin axis.

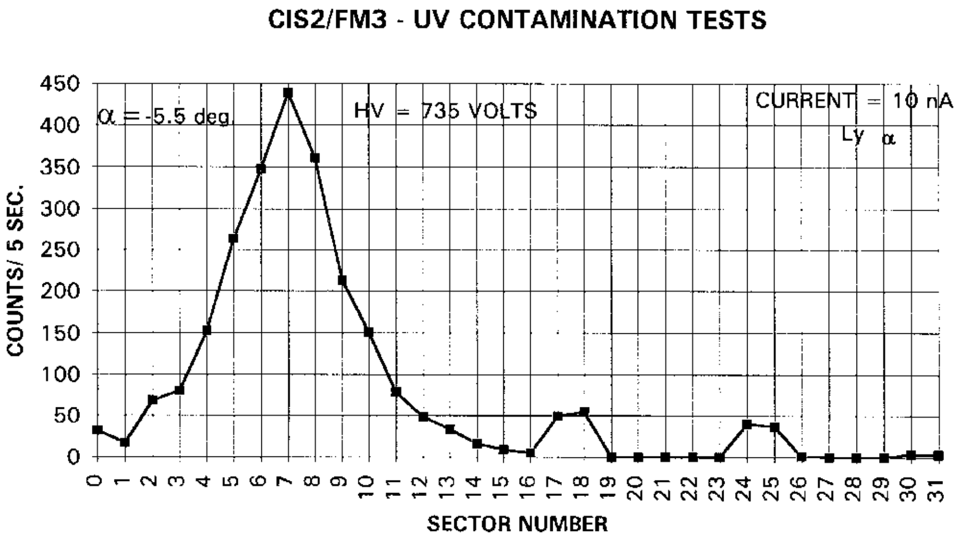

Figure 9. Azimuthal distribution of the solar UV count rate for each sector; the UV source is centered on sector 7 and the polar angle is $-5°$ (when the UV sunlight hits the inner hemisphere). Lα intensity measured by a windowless Au photodiode is equivalent to $\sim$3 Sun units.

To cover the large dynamic range required for accurate measurements in the low-density plasma of the magnetotail on the one hand and the dense plasma in the magnetosheath/cusp/boundary layer on the other, it is mandatory that CODIF employs two different sensitivities. The minimum number of counts in a distribution needed for computing the basic plasma parameters, such as the density, is about 100. These must be accumulated in 1 spin to provide the necessary time resolution. However, the maximum count rate which the time-of-flight system can handle is $\sim 10^5$ counts s^{-1} or 4×10^5 counts spin^{-1}. This means the dynamic range achievable with a single sensitivity is only 4×10^3.

Figure 1 shows the covered fluxes ranging from magnetosheath/magnetopause protons to tail lobe ions (which consist of protons and heavier ions); fluxes from $\sim 10^3$ to over 10^8 must be covered, requiring a dynamic range of larger than 10^5. This can only be achieved if CODIF incorporates two sensitivities, differing by a factor of 100. CODIF therefore will consist of two sections, each with 180° field of view, with different (by a factor of 100) geometrical factors. This way one section will always have count rates which are statistically meaningful and at the same time can be handled by the time-of-flight electronics. The exception is solar wind H^+ which will often saturate the instrument, but will be measured with HIA.

The CODIF instrument combines ion energy per charge selection by deflection in a rotationally symmetric toroidal electrostatic analyser with a subsequent time-of-flight analysis after post-acceleration to $\geq$20 keV e^{-1}. A cross section of the sensor showing the basic principles of operations is presented in Figure 10.

The energy-per-charge analyser is of a rotationally symmetric toroidal type, which is basically similar to the quadrispheric top-hat analysers. It has an uniform response over 360° of polar angle. The energy per charge selected by the electrostatic analyser E/Q, the energy gained by post-acceleration eU_{ACC}, and the measured time-of-flight through the length d of the time-of-flight (TOF) unit, τ, yield the mass per charge of the ion M/Q according to $M/Q = 2(E/Q + eU_{\mathrm{ACC}})/(d/\tau)^2\alpha$. The quantity α represents the effect of energy loss in the thin carbon foil ($\sim 3\ \mu$g cm^{-2}) at the entry of the TOF section and depends on particle species and incident energy.

3.1. Electrostatic Analyser Description

The electrostatic analyser (ESA) has a toroidal geometry which provides optimal imaging just past the ESA exit. This property was first demonstrated by Young *et al.* (1988). The ESA consists of inner and outer analyser deflectors, a top-hat cover and a collimator. The inner deflector consists of toroidal and spherical sections which join at the outer deflector entrance opening (angle of 17.9°). The spherical section has a radius of 100 mm and extends from 0 to 17.9° about the z-axis. The toroidal section has a radius of 61 mm in the poloidal plane and extends from 17.9° to 90°. The outer deflector covers the toroidal section and has a radius of 65 mm. The top-hat cover consists of a spherical section with a radius of 113.2 mm, which extends from 0 to 16.2°. It thus fits inside the entrance aperture of the outer deflector. The top-hat cover contains an O-ring outside the spherical section, which together with a lip on the outer deflector provides a seal of the sensor interior during integration and launch activities when the protection retractable cover will be closed. The outer

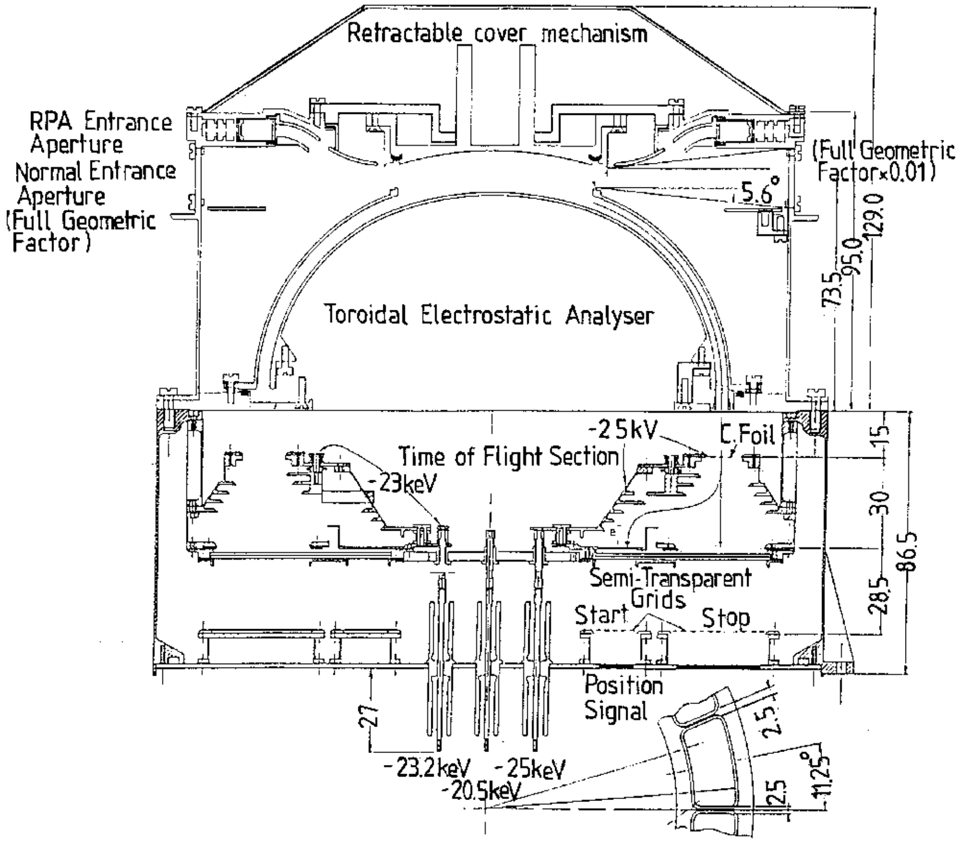

Figure 10. Cross-sectional view of the CODIF sensor. The voltages in the TOF section are shown for a 25 kV post-acceleration.

deflector and the top-hat cover will be at signal ground under normal operation, but will be biased at about -100 V during RPA operation. The inner deflector will be biased with voltages varying from -1.9 to -4950 V to cover the energy range in normal ESA operation and set to about -113 V for the RPA.

The fact that the analyser has complete cylindrical symmetry provides the uniform response in polar angle. A beam of parallel ion trajectories is focused to a certain location at the exit plane of the analyser. The exit position, and thus the incident polar angle of the ions, is identified using the information from the start detector (see Section 3.2) . The full angular range of the analyser is divided into 16 channels of 22.5° each. The broadening of the focus at the entrance of the TOF section is small compared to the width of the angular channels.

As illustrated in Figure 10, the analyser is surrounded by a cylindrical collimator which serves to define the acceptance angles and restricts UV light. The collimator consists of a cylindrical can with an inner radius of 96 mm. The entrance is covered by an attenuation grid with a radius of 98 mm which is kept at spacecraft ground. The grid has a 1% transmission factor over 50% of the analyser entrance and >95% transmission over the remaining 50%. The high transmission portion extends over the azimuthal angle range of 0 to 180° where 0° is defined along the spacecraft spin axis. The low transmission portion, whose active entrance only extends from 22.5° to 157.5° in order to avoid the counting of any crossover from the other half, has a geometric factor that is reduced by a factor of $\simeq$ 100 in order to extend the dynamic range to higher flux levels. On the low-sensitivity half, the collimator consists of a series of 12 small holes vertically spaced by approximately 1.9° around the cylinder. These apertures have acceptance angles of 5° FWHM, so there are no gaps in the polar angle coverage. The ion distributions near the polar axis are highly over-sampled during one spin relative to the equatorial portion of the aperture. Therefore, count rates must be weighted by the sine of the polar angle to normalise the solid-angle sampling for the moment calculations and 3D distributions.

The analyser has a characteristic energy response of about 7.6, and an intrinsic energy resolution of $\Delta E/E \simeq 0.16$. The entrance fan covers a viewing angle of 360° in polar angle and 8° in azimuth. With an analyser voltage of 1.9–4950 V, the energy range for ions is 15–40 000 eV e^{-1}. The deflection voltage is varied in an exponential sweep. The full energy sweep with 30 contiguous energy channels is performed 32 times per spin. Thus a partial two-dimensional cut through the distribution function in polar angle is obtained every $\frac{1}{32}$ of the spacecraft spin. The full 4π ion distributions are obtained in a spacecraft spin period. Including the effects of grid transparencies and support posts in the collimator each 22.5° sector has a respective geometric factor $A\Delta E/E\Delta\Theta\pi/8 = 2.16 \times 10^{-3}$ cm^{2}sr in the high sensitivity side and 2.3×10^{-5} cm^{2}sr where A denotes the aperture area and $\Delta\Theta$ the acceptance angle in azimuth. The acceptance in polar angle is $\pi/8$. The detection efficiencies of the time-of-flight system vary with particle energy, species and individual MCP assembly and therefore are treated separately in Section 3.5.

The outer plate of the analyser is serrated in order to minimize the transmission of scattered ions and UV. For the same reason the analyser plates are covered with a copper black coating. Behind the analyser the ions are accelerated by a post-acceleration voltage of 16–25 kV, such that also thermal ions have sufficient energy before entering the TOF section.

Retarding Potential Analyser

In order to extend the energy range of the CODIF sensor to energies below 15 eV e^{-1}, an RPA assembly is incorporated in the two CODIF apertures (see Figures 11 and 12). The RPA provides a way selecting low-energy ions as input to the CODIF analyser without requiring the ESA inner deflector to be set accurately near 0 V. The RPA collimates the ions, provides a sharp low-energy cutoff at a normal incident grid, pre-accelerates the ions to 100 eV after the grid, and deflects the ions into the ESA entrance aperture. The RPA will pass a 1 mm wide beam with

$\pm 5^{\circ}$ of polar angle range and to about 10° of azimuthal angle about the center axis of each of the entrance apertures over the 360° field of view, giving a geometric factor of 0.035 cm^2 sr. Collimation in azimuthal angle to $\pm 10^{\circ}$ of normal incidence to the RPA grid limits the entrance area to about half. The energy pass of the ESA is about 5–6 eV at 100 eV of pre-acceleration, assuming all deflection voltages are optimised. This energy pass is very sensitive to the actual RPA deflection optics, so that deflection voltages will have to be determined at about the 1% level.

The RPA consists of a collimator, RPA grid and pre-acceleration region, and deflection plates. The collimator section is kept at spacecraft ground.

The deflection system provides a method of steering the RPA low-energy ions into the CODIF ESA.

The RPA grid and pre-acceleration region consist of a pair of cylindrical rings, sandwiched between resistive ceramic material. Both inner and outer cylindrical rings contain apertures separated by posts every 22.5°, similar to the ESA collimator entrance, to allow the ions to pass through the assembly. The RPA grid is attached to the inner surface of the outer cylindrical ring. This outer ring has a small ledge which captures the RPA grid and which also provides the initial optical lens that is crucial to the RPA operation. Both inner and outer cylindrical rings are in good electrical contact with the resistive kapton (silver epoxy). During RPA operation the outer cylindrical ring is biased from spacecraft ground to about +25 V and provides the sharp low-energy RPA cutoff. This voltage is designated V_{rpa} in Figure 11. The inner cylindrical ring tracks the outer ring voltage and is biased at -100 V $+V_{rpa}$. The inner cylindrical ring, the ESA outer deflector, and the ESA top-hat cover are electrically tied to the RPA deflector.

The RPA deflection plates consist of three toroidal deflectors located above the ESA collimator entrance and one deflector disk located below the collimator entrance. The three toroidal deflectors are used to deflect the ions into the ESA. The deflector disk is used to prevent low-energy ions from entering the main aperture and to collect any photoelectrons produced inside the analyser, while in RPA mode.

3.2. Time-of-Flight and Detection System

The CODIF sensor uses a time-of-flight technology (Möbius *et al.*, 1985). The specific parameters of the time-of-flight spectrometer have been chosen such that a high detection efficiency of the ions is guaranteed. High efficiency is not only important for maximizing the overall sensor sensitivity, but it is especially important for minimising false mass identification resulting from false coincidence at high counting rate. Too thin a carbon foil would result in a significant reduction in the efficiency of secondary electron production for the ‘start’ signal, while an increase in thickness does not change the secondary electron emission significantly (Ritter, 1985). Under these conditions a post-acceleration of $\geq$20 kV is necessary for the mass resolution of the sensor.

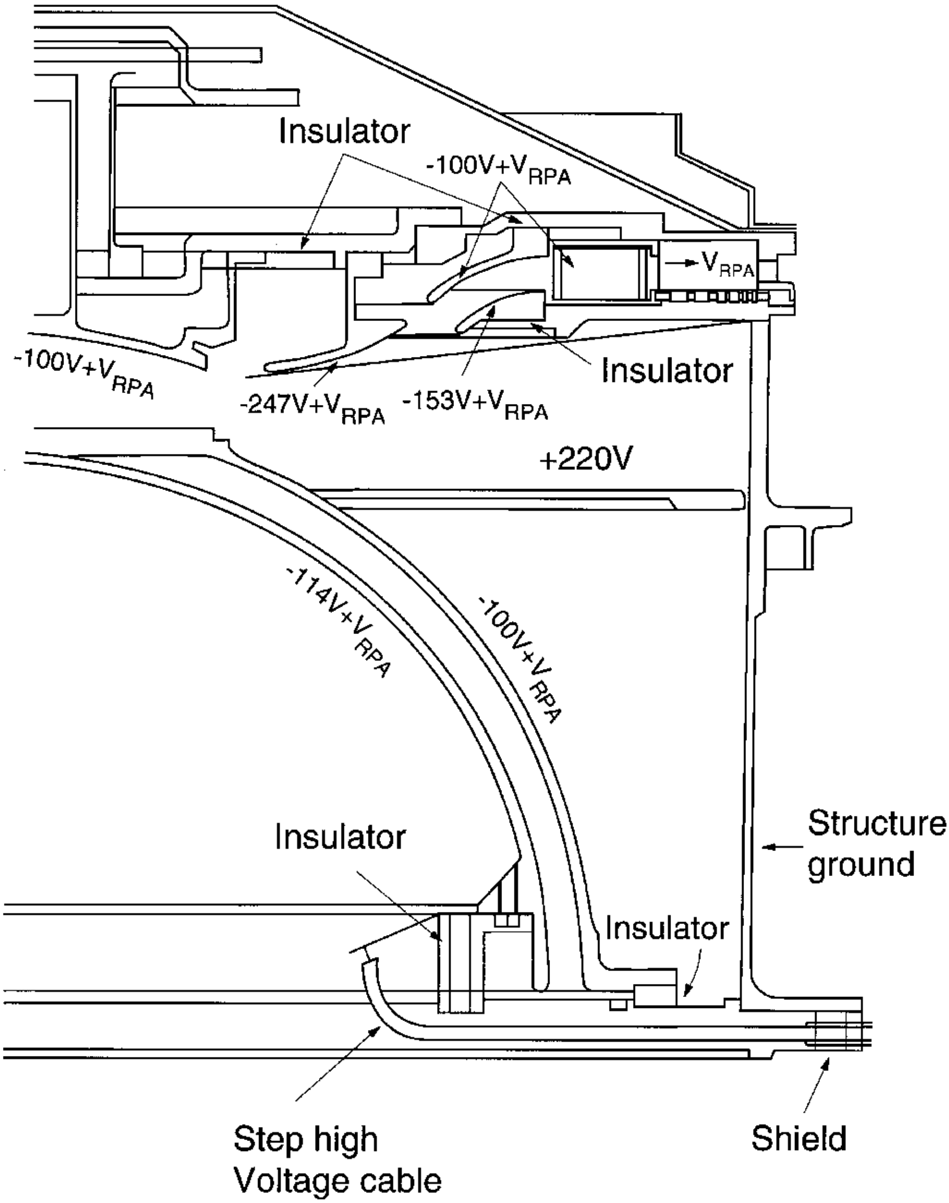

Figure 11. Geometry of the CODIF RPA.

After passing the ESA the ions are focussed onto a plane close to the entrance foil of the time-of-flight section (Figure 12). The TOF section is held at the post-acceleration potential (between -16 kV and -25 kV) in order to accelerate the ions into the TOF section with a minimum energy greater than 20 keV charge^{-1}. With this potential configuration the ion image on the foil extends from $r = 70$ mm

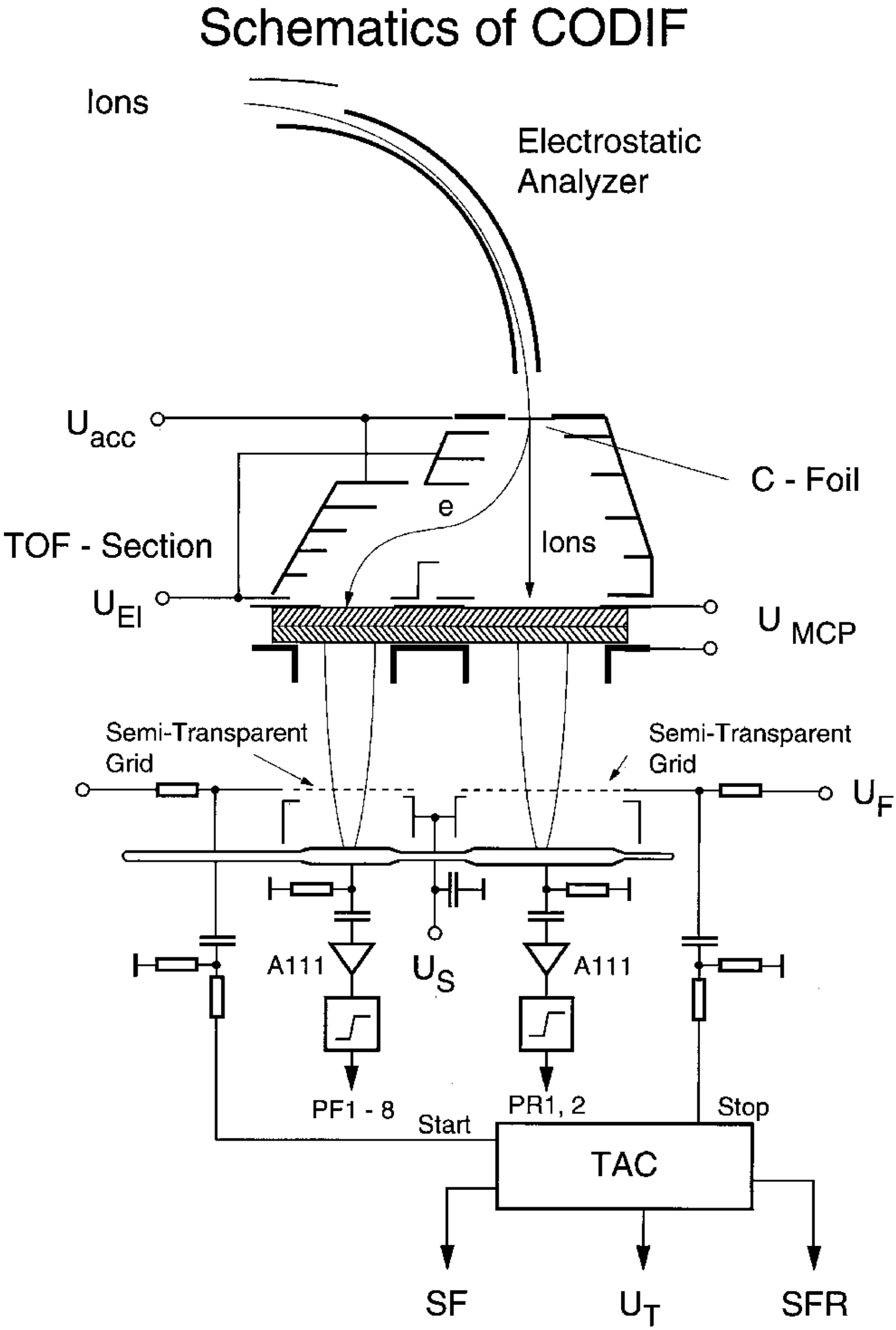

Figure 12. Schematics of CODIF sensor.

to $r = 80$ mm at high energies, and the image diameter is reduced to 3 mm or less at energies lower than 5 keV.

In the TOF section, the velocity of the incoming ions is measured. The flight path of the ions is defined by the 3 cm distance between the carbon foil at the entrance and the surface of the 'stop' microchannel plate (MCP). The start signal is provided by secondary electrons, which are emitted from the carbon foil during the passage of the ions. The entrance window of the TOF section is a 3 μg cm^{-2} carbon foil, which is an optimum thickness between the needs of low-energy loss and straggling in the foil and high efficiency for secondary electron production. The electrons are accelerated to 2 keV and deflected onto the start MCP assembly by a suitable potential configuration.

The secondary electrons also provide the position information for the angular sectoring. The carbon foil is made up of separate 22.5° sectors, separated by narrow metal strips. The electron optics are designed to strongly focus secondary electrons originating at a foil onto the corresponding MCP start sector.

Between the two sections with different geometrical factors a non-conducting plate with conducting strips in the appropriate equipotential configuration will ensure that no electrons and ions can penetrate into the other section.

The MCP assemblies are ring-shaped with inner and outer radii of 6×9 cm and 3×5 cm for the stop and start detectors, respectively. In order to achieve a high efficiency for the detection of ions at the stop MCP, a positive bias voltage is applied to collect secondary electrons from the 40% dead area of the MCP and the carbon foil.

The signal output of the MCPs is collected on a set of segmented plates behind the start MCPs (22.5° each), behind the stop MCPs (90° each), and on thin wire grids with ≈50% transmission at a distance of 10 mm in front of the signal plates, all being at ground potential (see Figure 10). Thus almost all of the post-acceleration voltage is applied between the rear side of the MCPs and the signal anodes. All signal outputs are coupled to 50 Ω impedance preamplifier inputs via a capacitor-resistor network. The timing signals are derived from the 50% transmission grids, separately for the high- and the low-sensitivity TOF section. The position signals, providing the angular information in terms of 22.5° sectors, are derived from the signal plates behind the start MCP.

Table I summarises the main performances of the HIA and CODIF sensors.

3.3. Sensor Electronics

The sensor electronics (Figure 13) of the instrument comprise two time-to-amplitude converters (TACs) to measure the time-of-flight of the ions between the start carbon foil and the stop MCPs, two sets of eight position discriminators at the start MCPs, two sets of two position discriminators at the stop MCPs, and the event selection logic. Each individual ion is pulse-height-analysed according to its time-of-flight,

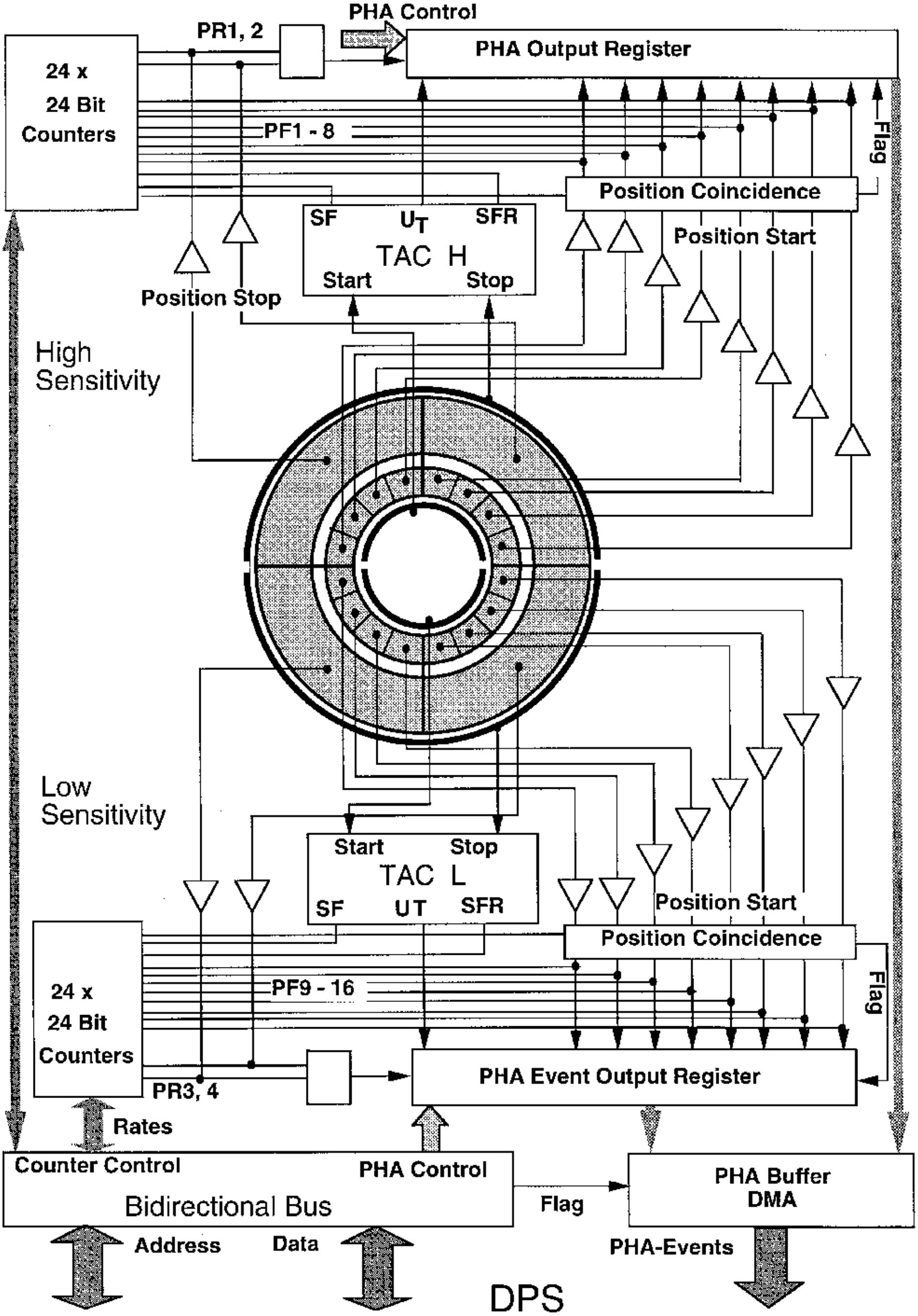

Figure 13. Functional block diagram of the CODIF sensor electronics.

incidence in azimuthal (given by the spacecraft spin) and polar angle (given by the start position), and the actual deflection voltage.

The eight position signals for each TOF section (in order to achieve the 22.5° resolution in polar angle) are independently derived from the signal anodes, while the timing signals are taken from the grids in front of the anodes. Likewise, the stop MCPs, consisting of four individual MCPs, are treated separately to carry along partial redundancy. By this technique the TOF and the position signals are electrically separate in the sensor. The position pulses are fed into charge-sensitive amplifiers and identified by pulse discriminators, the signal of which is directly fed into the event selection logic.

The TOF unit is divided into two TOF channels. The outputs of the 50% transmission grids in front of the signal anode of the MCPs are capacitively coupled to two input stages of the TOF electronics. These input stages consist of a preamplifier (rise time $<$0.9 ns) and a fast timing discriminator using a tunnel diode, and are contained in custom-made hybrids. The outputs of these hybrids are used to drive the TAC. The TAC provides an output signal whose amplitude is proportional to the time delay between the start and stop pulses. In addition, the TAC generates logical output signals for each start and stop pulse. The measured overall timing accuracy of the electronics for an amplitude of 100 mV of the start and stop pulse is 0.2 ns. The TAC output pulse is pulse-height analysed by a fast analog-to-digital converter (ADC) with a conversion time of $<$6 μs.

The conditions for valid events are established in the event-selection logic. The respective coincidence conditions can be changed via ground command. Several count rates are accumulated in the sensor electronics. There are monitor rates of the individual start and stop detectors to allow continuous monitoring of the carbon foil and MCP performance. The total count rates of TOF coincidence show the valid events accumulated for each TOF section. These rates can be compared with the total stop count rates in order to monitor in-flight the efficiency of the start and stop assemblies. There is a digital monitoring of all essential housekeeping values, like the deflection HVs, the post-acceleration voltage, the MCP HVs, and all the supply voltages of the electronics. In addition, the temperatures of the detector and electronics compartment are monitored. A simplified block diagram of the CODIF sensor electronics is presented in Figure 14.

In order to protect the MCPs, the solar-wind protons and the solar-wind alpha particles will be blocked from detection by a simple scheme during the sweeping cycle, as shown in Figure 15. The sweep, starting at high energies, is shown for the high-sensitivity section in the upper panel and for the low-sensitivity section in the lower panel in log E and azimuthal angle. The location of solar-wind protons and alphas in phase space is known from the HIA. By the use of this information the voltage sweep, which starts at high energies, is stopped above the alphas when the high-sensitivity section is facing the solar wind, and above the protons when the low-sensitivity section is facing the solar wind. The result is a small data gap for both sections of the sensor simultaneously. The primary purpose introducing

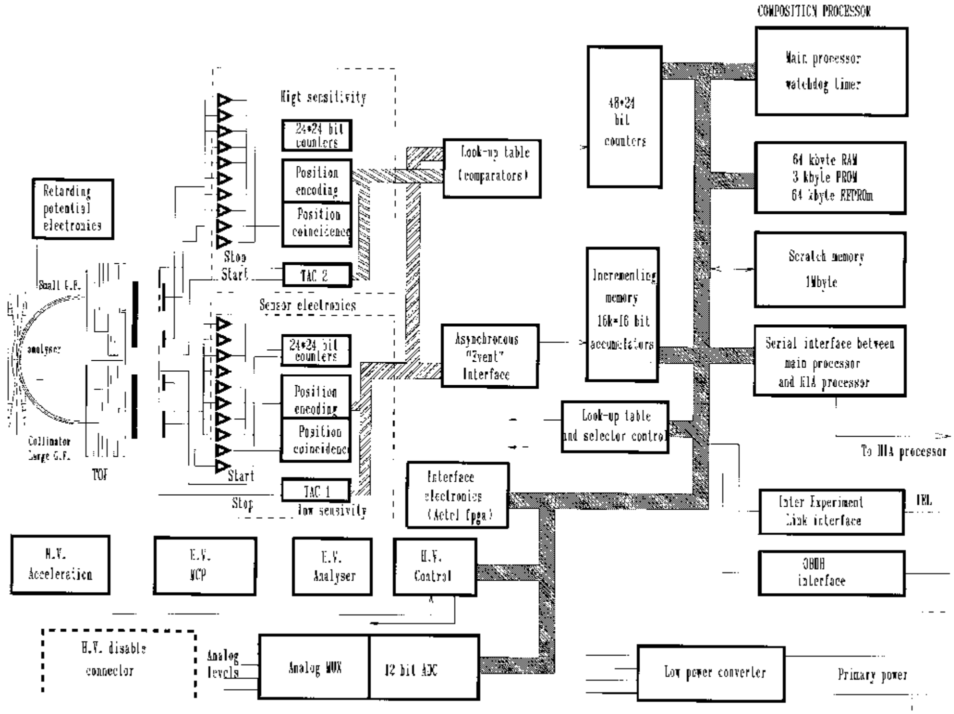

Figure 14. CODIF overall functional block diagram.

this scheme is to avoid short-time gain depression of the MCP area which would otherwise persist for the order of 1 s after the impulsive high count rate that would result from the solar wind.

3.3.1. *Counters and Incrementing Memory*

Each half of the CODIF sensor (high and low sensitivity) has eight angular bins and at least 64 TOF bins. A look-up table is used to combine TOF and energy into four mass species. The 32 combined mass/angle signals from each of the two parts of the analyser are sent into a selector circuit. The CODIF processor selects which part of the analyser is used. The 32 selected mass/angle signals feed the 48 counters, which are read out by the CODIF processor once per energy step. These counter values are used for moments, distribution functions, etc.

In addition to the counters, the CODIF has an incrementing memory accumulator used to make high-mass-resolution spectrograms. This memory can hold a full distribution (with limited angular resolution), so that long time averages can be made without using processor resources (memory, read-out time). According to the actual count rates, the CODIF processor selects which sensivity range (hence which half of the analyser) to accumulate. The TOF data from the selected half of the analyser are combined with the energy step and a look-up table and accumulated

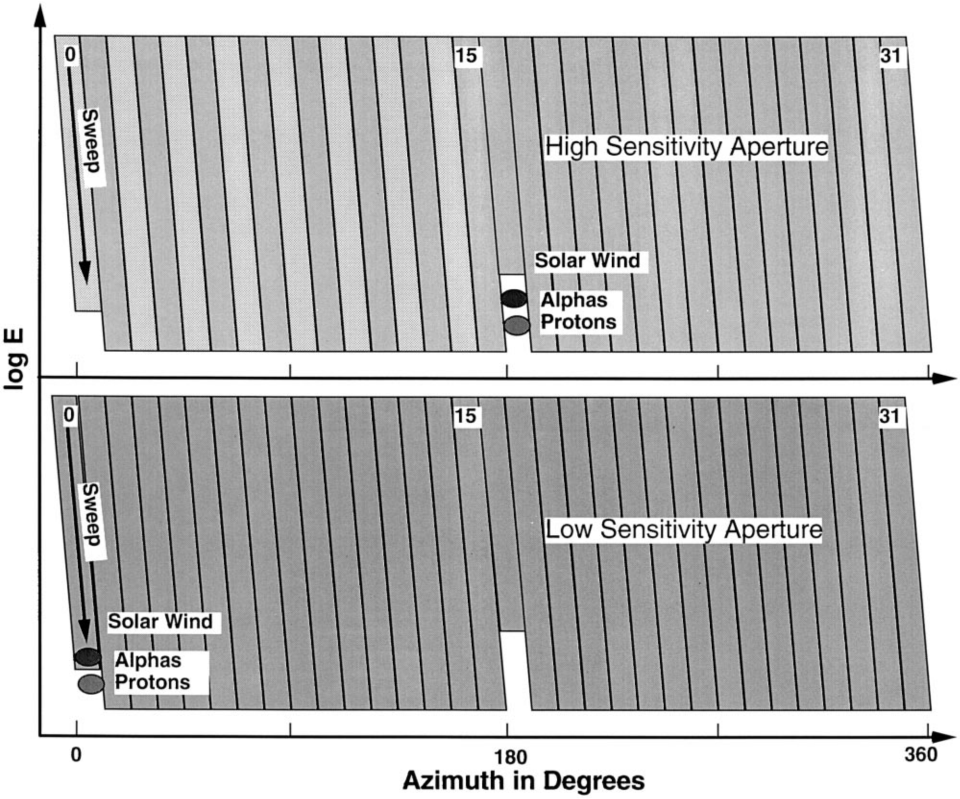

Figure 15. Energy sweeping scheme of CODIF in the solar wind. The sweep is shown in log E versus azimuthal angle for the high-sensitivity section (*upper panel*) and low-sensitivity section (*lower panel*), starting at the high energy end. When looking into the solar wind, the sweep stops above the alpha particles for the high-sensitivity section and above the protons for the low-sensitivity section.

into 64 mass channels. The eight angle bins from the selected half are combined with the spacecraft rotation sweep angle with another look-up table into 16 angular sectors with about 45° resolution. The 16 angles and 64 masses are combined with 16 energy bins to address the incrementing memory. The incrementing memory requires $16 \times 64 \times 16 = 16\,384$ accumulators.

3.3.2. *High Voltage System*

A sweep-voltage high-voltage power supply generates an exponential voltage waveform from 1.9 to 4950 V for the electrostatic analyser. A $\geq$20 kV static supply feeds the post-acceleration voltage, which can be adjusted via ground command. Another adjustable supply is used for the MCPs and the collection of secondary electrons. It supplies up to 5 kV and is floated on top of post-acceleration voltage. All high-voltage power supplies are run from the spacecraft raw power instead of from the low-voltage power converter. Thus the efficiency factor of the low-voltage power converter does not apply to the corresponding power consumption. Our design still garantees a galvanic separation of secondary and primary power.

3.4. Other elements

3.4.1. *Retractable Cover*

A retractable cover is used for CODIF, mainly to avoid carbon foil damage during launch operations.

3.4.2. *In-flight Calibration*

Routinely an in-flight-calibration (IFC) pulse generator stimulates the two independent TOF branches of the electronics according to a predefined program. Within this program all important functions of the sensor electronics and the subsequent on-board processing of the data can be automatically tested. Temporal variations of calibration parameters can be measured. The in-flight calibration can also be triggered by ground command in a very flexible way, e.g., for trouble shooting purposes. In addition, the known prominent location of the proton signal can, if necessary, serve as a tracer of changes in the sensor itself.

3.5. CODIF performances

3.5.1. *Resolution in Mass per Charge*

The instrumental resolution in mass per charge is determined by a combination of the following effects:

– energy resolution of the electrostatic deflection analyser ($\Delta E/E = 0.16$);

– TOF dispersion caused by the angular spread of the ion trajectories because of the characteristics of the analyser and the straggling in the carbon foil (the angular spread of $= 13^\circ$ leads to $\Delta\tau/\tau = 0.03$);

– TOF dispersion caused by energy straggling in the carbon foil ($\Delta\tau/\tau$ up to $= 0.08$ for 25 keV O^+);

– electronic noise in the TOF electronics and secondary-electron flight time dispersion (typically 0.3 ns).

The resulting TOF dispersion amount $\Delta\tau/\tau \leq 0.1$, which finally leads to a M/Q resolution between 0.15 for H^+ and 0.25 for low-energy O^+. A sample TOF spectrum for various 25 keV ions is shown in Figure 16 from calibration measurements with the CODIF sensor. It is demonstrated that all major ions are well separated by the sensor.

3.5.2. *Time-of-Flight Efficiency Curves*

The TOF efficiency is a function of the ion species and the total energy, the sum of the original ion energy plus the energy gained in the post-acceleration potential. The efficiency was also found to be a function of the position at which the ion enters the instrument. An efficiency versus energy curve is determined for each species, with an overall normalisation factor necessary for each azimuthal position. The

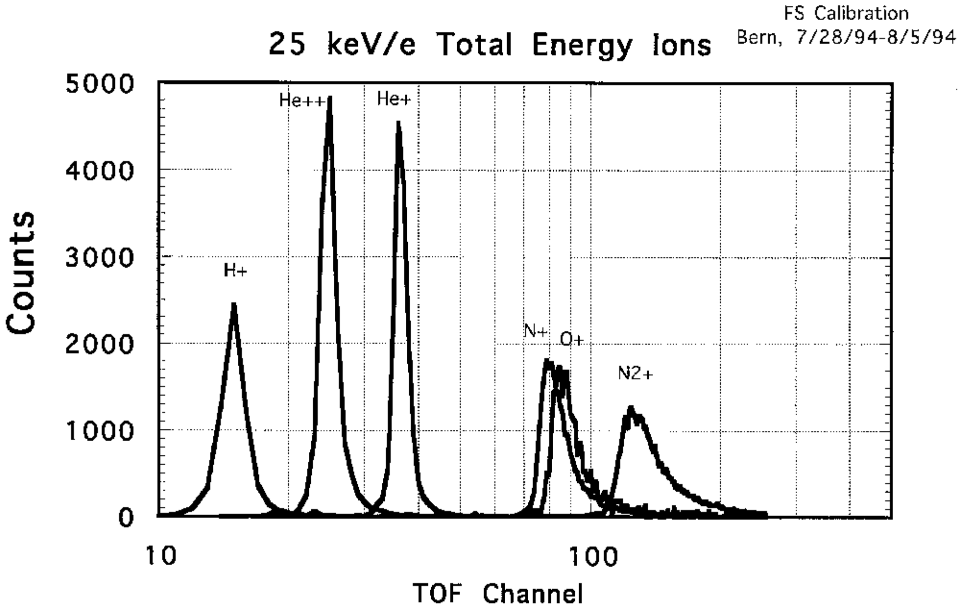

Figure 16. Time-of-flight spectrum of 25 keV H^+, He^{++}, He^+, N^+, O^+, and $N_2{}^+$ ions, as measured with the Flight Spare model of CODIF during a calibration at the University of Bern.

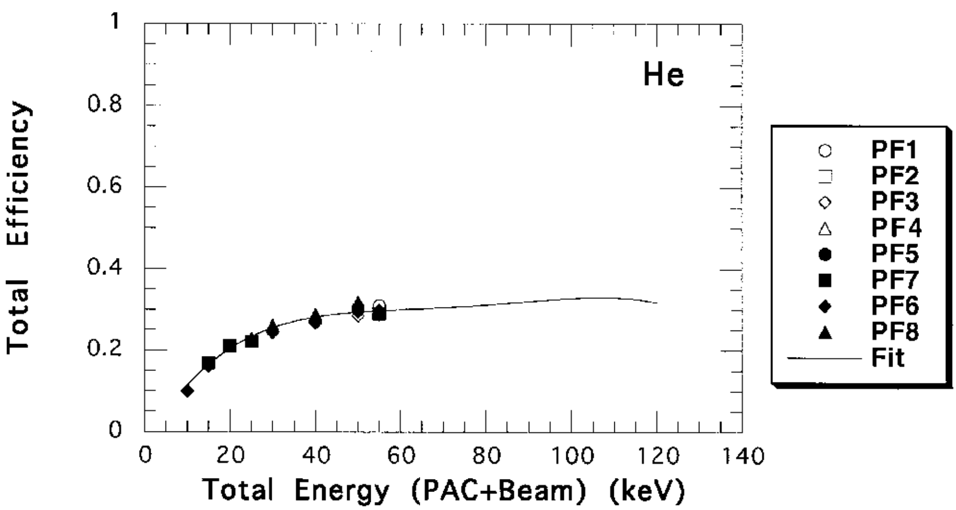

Figure 17. CODIF time-of-flight efficiency for Helium. PF1 through 8 indicate the individual angular sectors of 22.5° each of the high resolution side of the sensor.

efficiencies take into account the probability of getting a 'start' and 'stop' signal, plus the probability that an event will satisfy the valid event conditions. Figures 17 and 18 show the efficiency curves for He and for N^+. These curves were determined using data from Flight Model 1. Data from all positions on the high-sensitivity side

Table II
Total position adjustment for CIS flight model 1

Pixel	H^+	He	N^+
1.000	0.424	0.496	0.560
2.000	0.826	0.848	0.767
3.000	0.882	0.951	0.892
4.000	0.397	0.512	0.565
5.000	0.905	0.944	0.918
6.000	1.101	1.056	1.086
7.000	1.199	1.042	0.950
8.000	0.911	0.775	0.860
10.000	0.705	0.776	0.760
11.000	0.997	0.980	0.951
12.000	1.255	1.227	1.012
13.000	2.838	2.406	1.688
14.000	0.470	0.524	0.739
15.000	0.949	0.919	0.969

of the instrument are shown. The He curve is applicable to both He^+ and He^{++}. The N^+ and O^+ efficiencies are quite close, so the N^+ curve is used to represent the N^+ and O^+ group measured by the instrument. The final H^+curve has not yet been determined. Table II shows the position factors needed for each pixel and species for Flight Model 1. Note that this information is model-dependent, and this Table is shown just as an example of the amount of variablity that is observed.

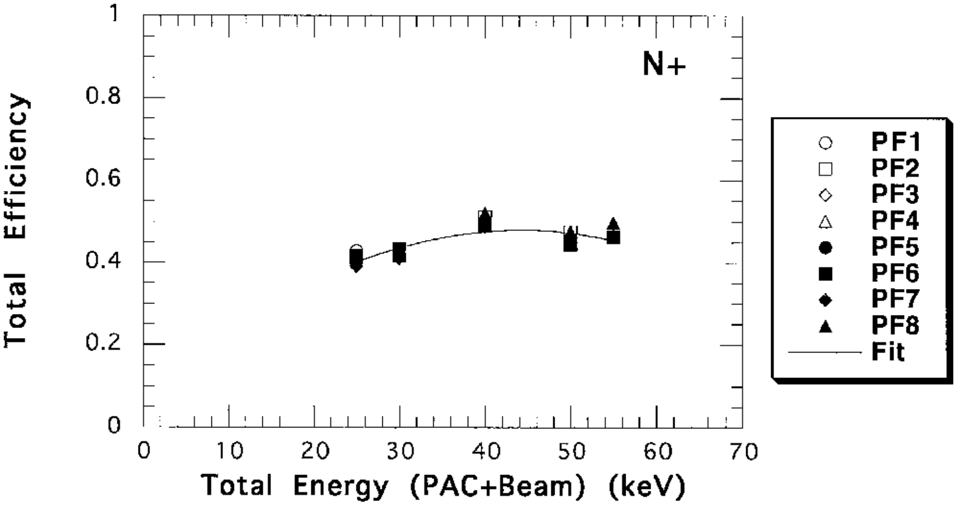

Figure 18. CODIF time-of-flight efficiency for N^+ ions.

3.5.3. *Immunity to Background*

Compared to a single detector instrument, the TOF sensors have an inherently better immunity to background, because of the start-stop coincidence requirement. The main source of background in these instruments is chance coincidence counts due to penetrating radiation and to events not detected by either start or stop MCP because detection efficiencies are less than 100% according to the relation:

$$R_{\mathrm{CHANCE}} = R^2_{\mathrm{SIGNAL}}\mu_1(1-\mu_2)\mu_2(1-\mu_1)\Delta\tau \ , \tag{1}$$

where R_{SIGNAL} is the input rate of the ion species with maximum flux, $\Delta\tau$ is the total TOF window, and μ_1 and μ_2 are the efficiencies of the start and stop assemblies, respectively. It can be easily seen that low efficiencies reduce the signal-to-noise ratio significantly. Therefore, great care has been applied to ensure as high efficiencies as possible for both start and stop detectors. The stop detector has an efficiency exceeding 90%. The efficiency of the start detector assembly is limited by the secondary electron emission of the foil. For protons of 25 keV the emission efficiency is reduced to $\sim$ 50% (Ritter, 1985). Similar values have been reached with the laboratory model of the sensor. Figure 19 shows the background-to-signal ratio versus incident proton flux level for 25 keV O^+ (the TOF window for the integration of counts is $\Delta\tau/\tau = 0.25$). It is demonstrated that the mass density of the plasma can still be determined with an accuracy of 10% (O^+/H^+ ratio better than 0.006) for proton fluxes as high as $= 10^8$ (10^{10}) ions s^{-1} cm^{-2} sr^{-1} with the full (or reduced) aperture, respectively.

A possible background due to UV photons is negligible, since the deflection plates are covered with copper black and photons undergo at least three scatterings before reaching the TOF system.

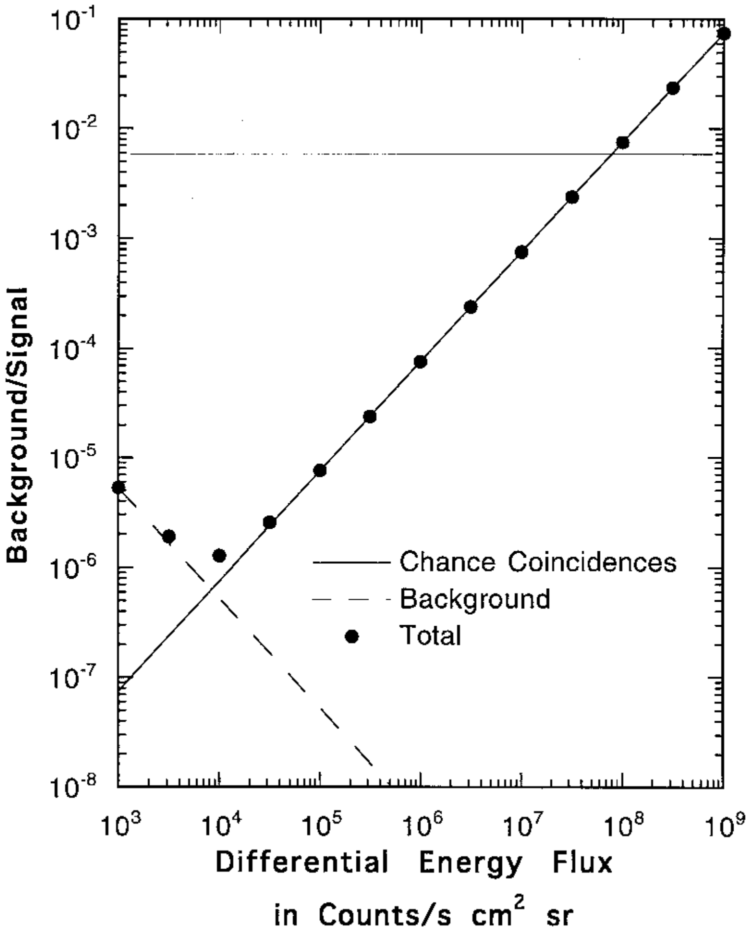

Figure 19. Background-to-signal ratio versus absolute proton flux for background due to chance coincidence of events creating only a start or a stop pulse (full line, computed for the actual start and stop efficiencies of CODIF). At low flux levels the background due to penetrating radiation and intrinsic effects of the MCPs prevails (broken line, taken from AMPTE SULEICA flight data (Möbius *et al.*, 1985)). The combination of both effects is shown by the solid circles. The horizontal line represents the limit for 10% accuracy of the mass density, if O^+ is the minor species.

3.5.4. *Dynamic Range*

The design of the electrostatic analyser guarantees a large geometrical factor in the high-sensitivity section $A\Delta E/E\Delta\tau\pi = 0.025$ cm^2 sr. The energy bandwidth is $\Delta E/E = 0.16$. The efficiency of the TOF unit is about 0.5. Differential energy fluxes as low as $\sim 3 \times 10^3$ ions s^{-1} cm^{-2} sr^{-1} can be detected by the instrument with the full time resolution of 1 spin period and about 5 counts energy^{-1} channel. The sensitivity is increased for longer integration time accordingly. Therefore the dynamic range reaches seven decades. The upper flux limit of the instrument amounts to 3×10^9 ions s^{-1} cm^{-2} sr^{-1}, which leads to a count rate of 10^5 counts s^{-1}

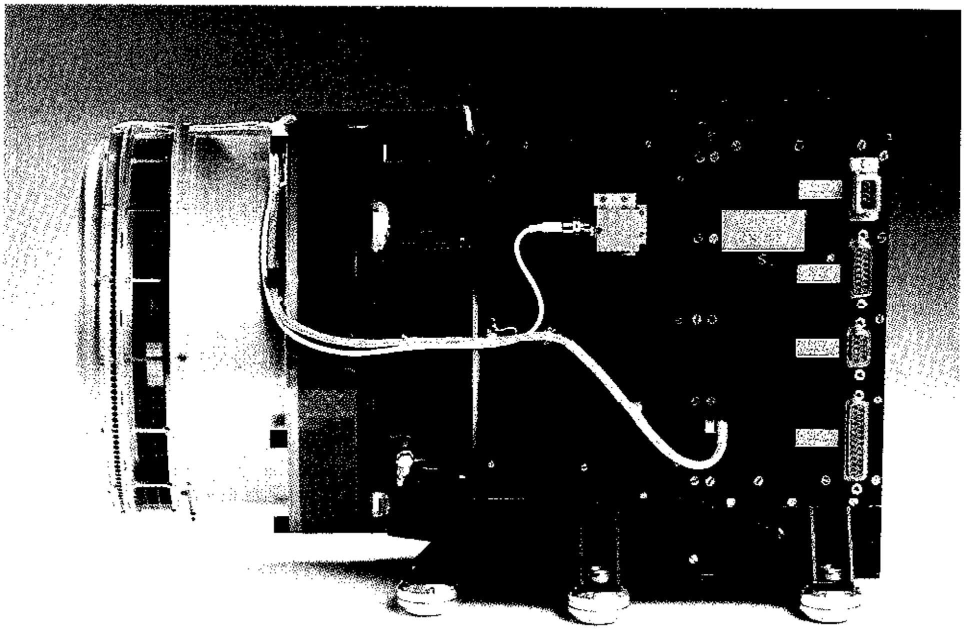

Figure 20. The CODIF sensor.

in one TOF unit (near saturation of the analysing electronics) and still guarantees a mass density determination to better than 10% accuracy for the reduced aperture geometry.

Performances of the CODIF sensor are summarised in Table I and in Figure 1. The full CODIF sensor is shown in Figure 20.

4. Data Processing System

4.1. On-board Data-processing System

Because of the high sensitivity and high intrinsic velocity-space resolution of the CIS instruments, continuous transmission of the complete 3D ion distributions sampled at the full time and angular resolution would require impossibly large bit rates. So, extensive on-board data-processing is a fundamental aspect of the CIS experiment. The CIS flight software has been designed to meet the scientific requirements of the mission even in limited transmission bit-rate allocation conditions.

First, the instrument data system (DPS) controls the operation and data collection of the two CODIF and HIA instruments, formats the data for the telemetry channel, and receives and executes commands. In addition, the DPS analyses and compresses on-board the tremendous amount of data to maximise the scientific return despite the limited CIS telemetry allocation. The DPS and the CODIF instrument are integrated in one box called CIS-1 and HIA is integrated in another box called CIS-2.

4.1.1. *Moments*

Moments of the distribution functions measured by the analysers will be computed by the DPS and continuously transmitted with maximum time resolution (1 spin period or 4 s). Main on-board calculated moments for CODIF and HIA instruments, to within a multiplicative factor dependent on the analyser geometrical factors, are given by the sums of Table III. These moments include particle density N_i (including partial densities over several energy ranges for CODIF, and sunward and anti-sunward densities for HIA), the three components of the flow vector V_i, the six unique components of the momentum flux tensor, and the heat flux vector. From these, the full pressure tensor can be deduced as well as the temperature anisotropies $T_{||}/T_{\perp}$. We anticipate that full 4π space coverage of the analysers and their clean response function will guarantee a high accuracy for the on-board computed moments. To calculate moments, integrals over the distribution function are approximated by summing products of measured count rates with appropriate energy/angle weighting over the sampled distribution. As already said, moments for HIA and for CODIF (for four masses) are computed once per spin.

Besides instrument sensitivity and calibration, the accuracy of computed moments is mainly affected by the finite energy and angle resolution, and by the finite energy range. The requirement on instrumental accuracy is best demonstrated in the measurements of mass flow through the magnetospheric boundary and in the computation of the current density in current layers like the magnetopause and the Flux Transfer Events (FTEs). Directional errors in the bulk velocity of less than 2° and relative errors less than 5% in the product of bulk velocity times number density of the different species are highly desirable. As for the mass flow, quantitative tests of other conservation laws (stress and energy balance) require measurements of plasma moments with uncertainties less than 5%. Paschmann *et al.* (1986) tested the capability of the AMPTE/IRM plasma instrument in a simulation study. For parameters typically observed in high-speed flow events, the simulation shows that density, velocity, temperature and pressure are accurately measured to within 5%. With the better azimuthal coverage and resolution of the CIS instruments, improved accuracy (in comparison to AMPTE/ IRM) of the plasma moments is expected (Martz, 1993). The accuracy requirements concerning the analysis of two- and three-dimensional current structures as well as shear and vortex flows, i.e. measurements strongly related to the four spacecraft aspect, are fulfilled by the capability of the instrument.

Table III
Moment definitions

To within a multiplicative factor dependent on the analyser geometric factor, the moments are given by the following sums:

Density:

$$N = \sum_E 1/V(E) \times \sum_\phi \sum_\theta C(\theta, \phi, E)$$

Bulk Velocity:

$$NV_x = \sum_E \sum_\phi \cos(\phi) \times \sum_\theta \cos(\theta) \times C(\theta, \phi, E)$$

$$NV_y = \sum_E \sum_\phi \sin(\phi) \times \sum_\theta \cos(\theta) \times C(\theta, \phi, E)$$

$$NV_z = \sum_E \sum_\phi \sum_\theta \sin(\theta) \times C(\theta, \phi, E)$$

Heat Flux Vector:

$$NH_x = \sum_E V^2(E) \times \sum_\phi \cos(\phi) \times \sum_\theta \cos(\theta) \times C(\theta, \phi, E)$$

$$NH_y = \sum_E V^2(E) \times \sum(\phi) \sin(\phi) \times \sum_\theta \cos(\theta) \times C(\theta, \phi, E)$$

$$NH_z = \sum_E V^2(E) \times \sum_\phi \sum_\theta \sin(\theta) \times C(\theta, \phi, E)$$

Pressure Tensor:

$$NP_{xx} = \sum_E V(E) \times \sum_\phi \cos^2(\phi) \times \sum_\theta \cos^2(\theta) \times C(\theta, \phi, E)$$

$$NP_{yy} = \sum_E V(E) \times \sum_\phi \sin^2(\phi) \times \sum_\theta \cos^2(\theta) \times C(\theta, \phi, E)$$

$$NP_{zz} = \sum_E V(E) \times \sum_\phi \sum_\theta \sin^2(\theta) \times C(\theta, \phi, E)$$

$$NP_{xy} = \sum_E V(E) \times \sum_\phi \cos(\phi) \times \sin(\phi) \times \sum_\theta \cos^2(\theta) \times C(\theta, \phi, E)$$

$$NP_{xz} = \sum_E V(E) \times \sum_\phi \cos(\phi) \times \sum_\theta \cos(\theta) \times \sin(\theta) \times C(\theta, \phi, E)$$

$$NP_{yz} = \sum_E V(E) \times \sum(\phi) \sin(\phi) \times \sum_\theta \cos(\theta) \times \sin(\theta) \times C(\theta, \phi, E)$$

where: E is energy

$\vec{V}$ is velocity

Θ, ϕ are the analyzer viewing angles

$C(\theta, \phi, E)$ are the measured counts

4.1.2. *Reduced Distributions*

Other reduced distributions, including pitch-angle distributions, averages (over 2 to 5 spin periods) or snapshots of the 3D distributions, will be computed with resolutions dependent upon the specific scientific objectives and telemetry rate. The two-dimensional pitch-angle distribution requires far less telemetry than the full distribution, thus allowing higher time resolution. Pitch-angle distributions can be transmitted when the magnetic field direction (provided on-board by the magnetometer) is in the field of view of the detector.

4.1.3. *On-Board Processing Unit*

Accomplishing these computations in real time is a heavy processing burden, and requires a sophisticated data system, both in terms of hardware and software. The data system is based on a set of two microprocessors (Figure 21). The main processor, located in the CIS-1 box, interfaces with the spacecraft On-Board Data Handling System (OBDH), the magnetometer, the plasma wave experiments (DWP), and the CIS-2 processor. It is in charge of formatting telemetry data, receiving and executing commands or passing them to the other processor, and controlling the burst memory. It also controls, collects and analyses data from the CODIF. The second processor is included in CIS-2 box and controls, collects and analyses data from the HIA. The main processor is interfaced with the second one by a serial data line; the HIA processor will compress the data so that the serial link can transmit at the highest data rates.

Each processor system consists of a Marconi MAS281 microprocessor, together with RAM, EEPROM and ROM memories, and a ‘watchdog’ timer. The ‘watchdog’ timer is used to monitor the health of the operation, software and reset the processor if the operation is abnormal. This allows the processors to recover automatically from transient problems such as radiation-induced single-event upsets. The software is designed to come up in a safe operating mode on reset. All hardware is radiation-hardened to the greatest extent possible, with spot shielding being used on any parts that are not sufficiently hard to withstand the Cluster environment.

4.1.4. *Scratch Memory*

The CIS experiment acquires data at nearly the fastest useful rate. In order to store a series of many two- and three-dimensional distributions at full time resolution, a 1 Mbyte memory is included in the instrument, so that discontinuities can be studied in detail.

4.2. TELEMETRY

4.2.1. *Data Products*

Tables IV and V give HIA and CODIF scientific telemetry products, respectively. Products consist of on-board computed moments, one-, two-, and three-dimenstional distributions and pitch-angle distributions. The high flexibility in

Table IV
HIA scientific telemetry products

Quantity	Product no.	Accum. Size	Basic Time (spin)	Total (bits)	bit/s
I. HOT POPULATIONS (large geometrical factor section)					
Moments $3\Delta\phi$(n,3v,6P,3H)	P2	468 words 16 spins 1 packet	1	468 x 16 + 32	117.5
Hot 3D Max Resolution (Large G Section) 62E x 8θ x 16ϕ	P5	3968 words 4 packets	1	63488 + 192	15920
3D 31E x 88Ω	P6	1364 words 2 packets	1	21824 + 96	5480
3D 31E x 42Ω	P7	651 words 1 packet	1	10416 + 48	2616
1D 62E	P9	8 spins 1 packet	1	496 x 8 + 32	125
1D 31E	P18	8 spins 1 packet	1	248 x 8 + 32	63
2D Azim. Distribution (integrated over polar angles) 31E x 16ϕ	P10	496 words 2 spins	1	3968 x 2 + 48	998
2D Polar Distribution (integrated over azim. angles) 31E x 16θ	P11	496 words 2 spins	1	3968 x 2 + 32	996
2D Polar Distribution 31E x 16θ for 3 sectors (solar wind, antisolar and flanks)	P20	1488 words 2 spins	1	11904 x 2 + 32	2976
2D Pitch Angle Distrib. Cut (2 slices/spin when B is in the field of view) 31E x 16θ x 2 slices	P12 P19	496 words 1 spin 2 spins	0.5 x 2 1	3968 x 2 + 48 3968 x 2 + 64	1996 1008
3D 16E x 88Ω	P15	704 words 1 packet	1	11264 + 48	2828
3D 30E x 88Ω	P16	1320 words 2 packets	1	21120 + 96	5304
3D 62E x 88Ω	P17	2728 words 3 packets	1	43648 + 144	10948
3D 31E x 8θ x 16ϕ (*)	P21	1984 words 2 packets	1	31744 + 96	7960
3D 31E x 8θ x 16ϕ compressed (**)	P23	992 words 2 packets	1	15872 + 5 x 2 x 16	4008

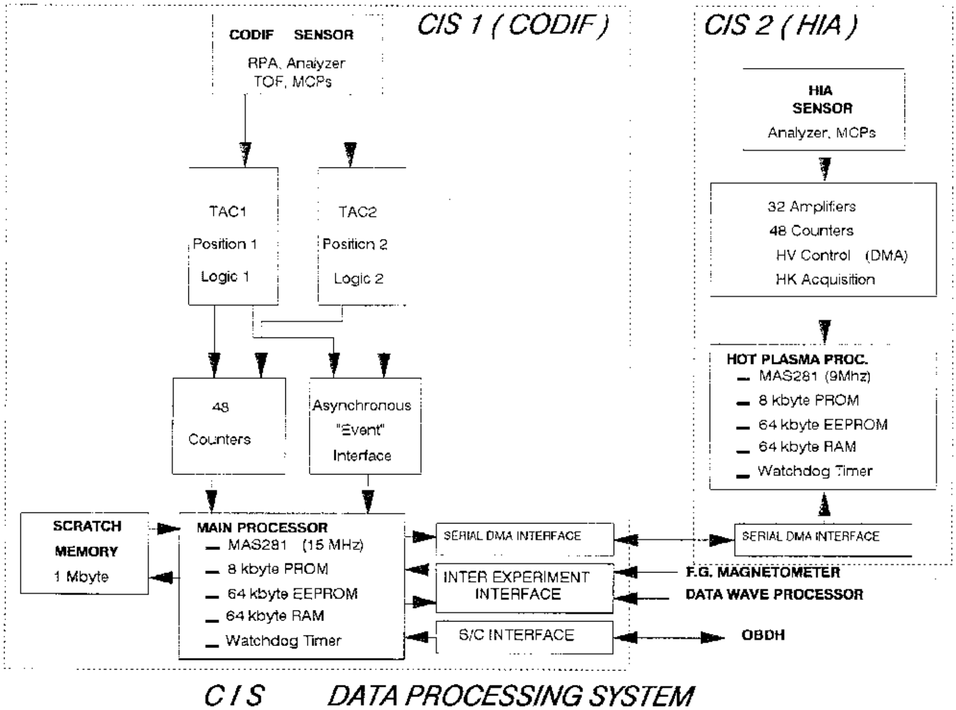

Figure 21. CIS data-processing system.

selecting data products to be transmitted at a given period depends upon the telemetry mode, bit rate sharing between CIS-1 and -2, and of course of the plasma environment; energy, angle, and time resolutions can be optimised to extract maximum information relevant to the scientific objectives. Data format changes are programmed within the instrument and do not require any reformatting of the spacecraft or ground data systems.

For example HIA produces typically a data volume of 32 polar sectors times 62 energies times 32 azimuth sectors, 16 bit-words, sampled in one spin period (4 s). Such a very high data rate has to be handled by a real-time operating system in order to elaborate and compress data to a few kbit s^{-1} telemetry stream output. All information is transmitted as log-compressed 8-bit-words, except moments which are transmitted with 12 bits. Pitch-angle distributions are instantaneous measurements when $\mathbf{B}$ is in the field of view of the instruments, and typical full 3D distributions are reduced to 88 Ω (solid angles) by taking into account oversampling in the polar regions.

A linear compression scheme is implemented as a part of the on-board CIS software, which allows the possibility to transmit compressed 3D distributions more often. The compression factor can be adjusted by setting new values to the compression parameters. A number of simulations have proven that a factor of

Table IV
Continued

Quantity	Product no.	Accum. Size	Basic Time (spin)	Total (bits)	bit/s
II. COLD POPULATIONS - SOLAR WIND (small geometrical factor section)					
Cold moments for solar wind $2\Delta E$ (n,3v,6P,3H)	P4	156 words 16 spins	1	312 x 16 + 16 x 18	82.5
3D 31E x 8θ x 8ϕ (cold 3D)	P8	992 words 1 packet	1	15872 + 32	3976
2D Cold Azim. Distrib. (θ integration) 31E x 8ϕ (5.6° each)	P13	496 words 4 spins	1	1984 x 4 + 32	498
2D Cold Polar Distrib. (ϕ) integration) 31E x 8θ (5.6° each)	P14	496 words 4 spins	1	1984 x 4 + 32	498
3D 31E x 8θ x 16ϕ (*)	P22	1984 words 2 packets	1	31744 + 32	7944
3D 31E x 8θ x 16ϕ compressed (**)	P24	992 words 1 packet	1	15872 + 4 x 16	3984

ϕ: azimuthal angle
θ: polar angle
Ω: solid angle

Packet header: 2 x 16 bits = 32 bits
Frame Header: 9 x 16 bits = 144 bits / 5.1522 sec *(duration independent of the TM mode)*
1 word = 16 bits

*: calibration products
**: compression $\geq$ 2 (2.5 should be expected; 2 assured)

two in the compression factor can easily be reached without any loss of data. The chosen algorithm for this compression is based on the evaluation of the dispersion of the maximum of a data token around the average of the data token itself. If the maximum (Max) satisfies the following:

$$\mathrm{Max} - k^*\sqrt{(\mathrm{Max})} < \mathrm{Token}_{\mathrm{Average}} ,$$

where k is an ajustable parameter factor to set the dispersion, the data are assumed to be equal to the $\mathrm{Token}_{\mathrm{Average}}$ which is transmitted as representative of the whole token. Otherwise the token length is scaled by a factor two and the above inequality is applied until the relation is satisfied or the token length has been reduced to one. If k is assumed to be 0 the compression becomes error-free.

Basically, for HIA, the high-sensitivity section has full 180° coverage and hot population data are computed using data from this section. When there is a cold

Table V
CODIF scientific telemetry products

Quantity	Product no.	Packet numbers	Basic Time (spins)	Total (bits)	bit/s
I. HOT POPULATIONS					
Moments 3ΔE(n,3v,6P,3H) x 4M	P7	1	1	1872 + 32	476
3ΔE (Heat Flux Tensor, 7 more components) x 1M	P8	1	1	252 + 32	71
3D 64M x 8E x 6Ω *(6Ω : 2 polar, 4 perpendicular)*	P11	2	2	24576 + 64	3080
3D 4M x 31E x 88Ω (*) **	P13 + P16 + P18	7	1	87296 + 224	21880
3D 4M x 16E x 88Ω (*) **	P12 + P15 + P17	4	1	45056 + 128	11296
3D 1M x 31E x 24Ω	P14	1	1	5952 + 32	1496
2D PAD Cut 4M x 31E x 8θ *(2slices/spin when B is in the field of view)* *	P24	1/slice	0.5	7936 x 2 + 2 x 32	3984
2D PAD Cut 4M x 16E x 8θ *(2slices/spin when B is in the field of view)***	P23	1/slice	0.5	4096 x 2 + 2 x 32	2064 (1032/slice)
2D 4M x 31E x 16ϕ * 2D 2M x 16E x 16ϕ (protons + α) ** or 4M x 16E x 8ϕ **	P19 P21 P20	1 1 1	1 1 1	15872 + 32 4096 + 32 4096 + 32	3976 1032 1032
2D 1M x 31E x 32ϕ	P22	1	1	7936 + 32	1992
90° PAD 2M x 4β x 4E	P25	1	1	256 + 32	72
Live Pulse Height Data Time of flight: 8 bits Azim. Position: 5 bits Energy Step: 7 bits Sector: 3 bits Proton mode: 1 bit	P28	1		24 x k + 32 every 2 spins k > 1	depending of k value
Monitor Counting Rates 16 signals x 16E x 16ϕ	P27	4	32 spins	32768 + 128	257
II. RPA MODES					
RPA diagnostic product 4M x 31E x 88 Ω x 4 sweeps	P29	1	75	349184 + 32	1164
RPA Science product 4M x 8E x 9Ω + 1 start energy for each mass 5 bits + 1 start angle for each mass 7 bits	P30	1	1 spin every N spins	2316 + 32	587/N
RPA Moments	P31	1	1	624 + 32	164
III. COLD POPULATIONS					
Cold Populations Moments 3ΔE(n,3v,6P,3H) x 4M 3ΔE (Heat Flux Tensor, 7 more components) x 1M	P9 P10	1 1	1 1	1872 + 32 252 + 32	476 71
Solar Wind Helium + Proton Tail 2M x 8Ω x 8E	P26	1	1	1024 + 32	264

ϕ: azimuthal angle (spin phase angle)
θ: polar angle
Ω: solid angle
β: near 90° pitch angles (the highest possible angle) for gyrotropic distributions (for 4 high energies)
4M: protons, α + 2 other masses

* best possibility
** basic use
(*) possibility to have different time of resolution for the different masses

Packet Header: 32 bits

population like the solar wind, the rest of the spin (360°–45°) is not be ignored, but, using the large geometrical factor section, data are taken and transmitted.

For CODIF, 4M stands for the four major species: H^+, He^{++}, O^+, and He^+. 64M 3D distributions can be read out at a slow rate. They give more detailed information about the presence of minor species. 4M, 88 Ω (solid angles), 3D distributions should be read out as often as possible, after all the other data types have been accommodated. A priority scheme for the time resolution is given according to the abundance of the species:

H^+ highest resolution,
He^{++} or O^+ highest resolution or slower by a factor of 2,
He^+ or other species factor of 2 or factor 4 slower.

4.2.2. *Remote-sensing Distribution*

Close to boundaries a distribution of four angles at 90° pitch-angle (phase 0°, 90°, 180°, 270°) is accumulated for two species (H^+ and O^+) in the four highest energies. This allows the boundary motions to be traced.

4.2.3. *Live Pulse Height Data*

For each particle CODIF measures the following parameters:

Time-of-flight:	8 bits	(giving 256 values)
Azimuthal position:	5 bits	(32 sectors)
Proton mode:	1 bit	
Energy step:	7 bits	(one between 128 elementary steps)
Pixel number:	3 bits	
Total:	24 bits each	

4.2.4. *Monitor Rates*

To check the performance and the counting efficiency of CODIF certain monitor rates have to be accumulated and transmitted with the science data:

2 Start	(each time-to-amplitude converter)
2 Coincidence	(each time-to-amplitude converter)
16 Start position	
4 Stop position	

To cut down in bit rate a specific scheme is proposed by which only every fourth energy step and every eighth sector are transmitted at a time. A cycle is completed after 32 spins.

4.2.5. *Telemetry Formats*

Instrument science and housekeeping data are read out over a single serial interface; the two types are differentiated by separate word gates. Telemetry is collected as a series of blocks, a fixed number per telemetry frame. Telemetry frames are always 5.152222 s in duration independent of telemetry mode, and are synchronised by a ‘Reset’ pulse that occurs at the beginning of each frame. Housekeeping data consists of 54 bytes per telemetry frame. Science can be collected in a variety of modes with different bit-rates; these modes are subdivided into ‘Normal’ and ‘Burst’ Modes, differentiated by the number of blocks per frame (10 for normal and 62 for burst). The different bit rates for Normal Mode are generated by changing the number of words per block.

Mode	Name	Bit s^{-1}	Block size	Blocks/frame	Bytes/frame
NM1	Normal mode	5 527	356	10	3 560
NM2	Ion mode	6 521	420	10	4 200
NM3	Electron mode	4 503	290	10	2 900
BM1	Normal burst mode	26 762	278	62	17 236
BM2	WEC/WBB TR mode	6 546	68	62	4 216
BM3	Event memory readout	29 456	306	62	18 972

BM3 is a special mode to dump the instrument scratch memory only; it is not an ordinary operating mode.

Two contingency modes exist in which all available data will go either to CIS-1 (CODIF) or to CIS-2 (HIA).

The four Cluster spacecraft will fly through a number of different plasma environments, and there must be a mechanism to change the mode of the instrument with a minimum number of commands when moving from one region to another. The CIS instruments have a large amount of flexibility either in the selection of the operating mode and in the reduction of the data necessary to fit the available telemetry bandwith. The instrument must be capable of making many changes to the operational details in response to a few commands.

Table VI shows the 16 CIS basic operation modes with the bit-rate sharing between CODIF and HIA, defined for each spacecraft bit-rate mode. The CIS instruments will operate in the different regions of the Earth’s environment in these 16 operative modes that, for the five telemetry regimes foreseen (forgetting HK and BM3 modes), give a total amount of 80 science data transmission schemes. Each basic scheme corresponds to a given sequence of products, spanning from the momenta of the ion distributions to the 3D.

Roughly speaking, all these 16 operative regimes can be grouped into solar-wind tracking oriented modes, solar-wind study modes with the priority on the backstreaming ions, magnetospheric modes, an RPA mode and a calibration mode. Moreover, part of these solar-wind and magnetospheric modes are duplicated in a similar mode in which 3D compression is introduced.

For the HIA instrument two basic modes of operations, mixing basic products defined in Table IV have been implemented according to the plasma populations

Table VI
CIS operation modes

			TELEMETRY MODE CIS-2 BITRATE (bit/s)				TELEMETRY MODE CIS-1 BITRATE (bit/s)			
MODE		**Mode Name**	**NM1**	**NM2**	**NM3**	**BM1**	**NM1**	**NM2**	**NM3**	**BM1**
0	SW-1	SOLAR WIND / SW tracking	1 272	1 272	1 272	7 000	4 255	5 252	3 231	19 762
1	SW-2	SOLAR WIND / 3D backstreaming ions	1 272	1 272	1 272	7 000	4 255	5 252	3 231	19 762
2	SW-3	SOLAR WIND / SW tracking	2 135	2 135	2 135	13 162	3 392	4 386	2 368	13 600
3	SW-4	SOLAR WIND / 3D backstreaming ions	2 135	2 135	2 135	13 162	3 392	4 386	2 368	13 600
4	SW-C1	COMPRESSION SW-3 (+3Ds) solar wind tracking	2 135	2 135	2 135	13 162	3 392	4 386	2 368	13 600
5	SW-C2	COMPRESSION SW-4 (+3Ds) backstreaming ions	2 135	2 135	2 135	13 162	3 392	4 386	2 368	13 600
6		RPA								
7	PROM	PROM OPERATION								
8	MAG-1	MAGNETOSPHERE 1	1 272	1 272	1 272	7 000	4 255	5 252	3 231	19 762
9	MAG-2	MAGNETOSPHERE 2	2 135	2 135	2 135	13 162	3 392	4 386	2 368	13 600
10	MAG-3	MAGNETOSPHERE 3	3 124	4 148	2 135	13 162	2 403	2 373	2 368	13 600
11	MAG-4	MAG-1 SHEATH/TAIL	1 272	1 272	1 272	7 000	4 255	5 252	3 231	19 762
12	MAG-5	MAG-2 SHEATH/TAIL	2 135	2 135	2 135	13 162	3 392	4 386	2 368	13 600
13	MAG-C1	COMPRESSION MAG-1 + 3Ds	1 272	1 272	1 272	7 000	4 255	5 252	3 231	19 762
14	MAG-C2	COMPRESSION MAG-4 + 3Ds sheath/tail	1 272	1 272	1 272	7 000	4 255	5 252	3 231	19 762
15	CAL.	CALIBRATION								

CIS (HIA + CODIF):
NM1: 5527 bit/s
NM2: 6521 bit/s
NM3: 4503 bit/s
BM1: 26762 bit/s

Normal modes: NM1 or BM1

Baseline is to have identical modes on the 4 spacecraft

encountered along the Cluster orbit: so-called (a) ‘magnetospheric’ modes, and (b) ‘solar-wind’ modes. In both modes moments are systematically transmitted, computed every spin from the data acquired on the high-sensitive half-hemisphere (‘high G’ section) when the spacecraft are inside the magnetosphere, from the attenuated half-hemisphere section (‘low g’) when the spacecraft are in the interplanetary medium. This way one of the goals of the mission, i.e., to be able to produce high-resolution (4 s) moments by on-board computation, has been fullfilled for all the listed regimes apart from the calibration mode. The computed moments are used on-board to drive automatic operative mode changes (when this option has been remotely enabled) to better follow fluctuations which require fast-sensitivity-adapting capabilities or to select the best energy sweep regime to cover the local solar wind distribution.

‘Magnetosphere’ basic modes stay relatively simple, i.e., the full energy-angle ranges are systematically covered and the different data products (including moments) are deduced from the 62E $\times$ 88Ω energy solid angle count rate matrices accumulated on the ‘high G’ section.

‘Solar wind’ modes allow a precise and fast measurement (4s) of the ion flow parameters (H^+, He^{++}). For that, in the solar wind, the sweep energy range is automatically reduced and adapted every spin, centred on the main solar wind velocity by using a criterion based on the H^+ thermal and bulk velocities computed during the previous spin. Moreover, detailed 3D distributions (e.g., for upstreaming ions and/or for interplanetary disturbances) are included in the basic products transmitted to the telemetry.

In both regions, and within the HIA telemetry allocation, a maximum bit rate has been allowed for transmission as often as possible of full size (or reduced) 3D distributions. From Table VII it can be anticipated that Burst Modes should be considered as those having the highest expected scientific return.

Finally, to best fit the sampling activity to the plasma environment, if an auto-switching variable has been asserted, it is possible to run the instrument in the auto-change mode from magnetospheric to solar-wind configuration and *vice versa*. The switching criteria are presently based on locally measured plasma Mach number checks.

Science data packets include a number of data products from both HIA and CODIF in a flexible format. Data are time-tagged in such a way as to allow absolute timing of the data on the ground. The format allows bit rate allocations to the various data products to be changed relatively easily with minimal impact on ground processing. All auxiliary data necessary to analyse the data, such as instrument operational mode and timing information, are included in science data products, as it could be difficult to recombine housekeeping packets with the science packets.

Finally, housekeeping data (81 bit s^{-1}), extensively used during spacecraft development tests, give all the information needed to follow the health and safety of the instrument.

Table VII

Examples of basic operational modes of the CIS-2 (HIA) experiment grouped in 4 tables according to the space region of interest. For each telemetry mode (NM1, NM2, ...) different combinations of scientific products (see their definition in Table IV) are defined, computed from count rates provided by the high-sensitive half analyser ('high G' section) and/or the low geometrical factor half ('low g' section). Each basic mode (MAG-1, MAG-2, ..., SW-2, SW-3, ...) in a given telemetry mode refers to Table VI.

MAGNETOSPHERIC MODES						HIGH G SECTION							
TELEMETRY MODE				HIA Bit rate (bit/s)		M	1D	2D			3D		
OPERATION MODE						P2	P9	P10	P11	P12	P6	P15	P17
NM1	NM2/BM2	NM3	BM1	Alloc.	HIA	Mom.	62E	2Dφ AZ	2Dθ POL	2DαPAD	31Ex88Ω	16Ex88Ω	62Ex88Ω
5527	6521/6546	4503	26762			117.5	125	998	996	1996/1008	5480	2828	10948
MODES 8-11				1272	1186							3 sp	
MODES 6-9-12				2135	2070						3 sp		
MODE 7				2135	2112								
10				3124	3071							1 sp	
	MODE 10			4148	4079					1 sl.			
			6-7-8-11	7000	6731					1 sl.			
			9-10-12	13162	13062					2 sl.			

SOLAR WIND MODES						HIGH G SECTION					Low g SECTION			
TELEMETRY MODE				HIA Bit rate (bit/s)		1D	2D		3D		M	2D		3D
OPERATION MODE						P18	P10	P20	P6	P15	P4	P13	P14	P8
NM1	NM2/BM2	NM3	BM1	Alloc.	HIA	31E	2DφAZ	2DθPOL	31Ex88Ω	16Ex88Ω	M	2Dθ POL	2Dφ AZ	31Ex8θx8φ
5527	6521/6546	4503	26762			63	998	2976	5480	2828	82.5	498	498	3976
MODE 0				1272	1275		5 sp							/4 sp
MODE 2				2135	2141									/2 sp
			0-6	7000	6869				2 sp					
			MODE 2	13162	12531									
MODE 1				1272	1088					3 sp				/18 sp
MODE 3				2135	2074				3 sp			/2 sp		/18 sp
			MODE 1	7000	6307									/5 sp
			MODE 3	13162	6464									/15 sp

COMPRESSION MAGNETOSPHERE						HIGH G SECTION				
TELEMETRY MODE				HIA Bit rate (bit/s)		M	3D			
OPERATION MODE						P2	P6	P15	P17	P23
NM1	NM2/BM2	NM3	BM1	Allocated	HIA	Moments	31Ex88Ω	16Ex88Ω	62Ex88Ω	31Ex8θx16φ
5527	6521/6546	4503	26762			117.5	5480	2828	10948	3206 [COMP=2.5]
MODES 13-14				1272	~1270					~ 3 sp

COMPRESSION SOLAR WIND						HIGH G SECTION	Low g SECTION		
TELEMETRY MODES				HIA Bit rate (bit/s)		3D	M	2D	3D
OPERATION MODES						P23	P4	P13	P24
NM1	NM2/BM2	NM3	BM1	Allocated	HIA	31Ex8θx16φ	Moments	2Dθ POL	31Ex8θx8φ
5527	6521/6546	4503	26762			3206 [COMP=2.5]	82.5	498	1992 [COMP=2]
MODE 4				2135	~2135				
MODE 5				2135	~2135	2 sp.			/16 sp.

3 sp.: integrated over 3 spins /3 sp.: once every 3 spins 1,2 sl.: 1 or 2 slices

Table VII shows the scientific products of HIA transmitted nominally in the various telemetry modes.

4.3. Modes of operation

4.3.1. *Telemetry*

One of the decisive variables which affects the instrument operation is the telemetry mode; when the telemetry mode changes, the CIS instrument receives a single command and changes accordingly its bit rate allocation and data product collection mechanism to match the available telemetry. Some instrument parameters stay mode-independent and are programmable, such as MCP voltage.

The DPS is made of a small PROM, some EEPROM, and some RAM memories. The non-volatile EEPROM memory contains most of the on-board code and parameter tables, the RAM memory is used primarily to hold data blocks and some operational parameters and the PROM memory contains the bootstrap code needed to load or change the EEPROM. The EEPROM memory cannot be read while it is being programmed, and programming takes several millisec per block; it contains most of the operational parameters so that they do not have to be reloaded on power-up.

As a basic philosophy the default operational parameters are kept in EEPROM memory, while the current operational parameters are in RAM memory. The telemetry mode independent parameters are copied from the defaults on processor reset (this is called the 'Fixed Table'). The 'Operational Mode Table' is copied from the default table to set up a new mode after commanding. Sometimes it may also be desirable to follow automatic operational mode changes based only on science data (e.g., moments) collected by the instrument. The 'Telemetry Allocation Table' is a subset of the Operational Mode default Table; when the telemetry rate changes, the appropriate Telemetry Allocation Table is copied from the default table for the new rate and the current operational mode.

The CIS-1 and CIS-2 instruments have separate tables, but of course are controlled by the same telemetry rate and operation mode commands.

4.4. Ground science data processing

The CIS raw telemetry will be pipeline-processed at the French Cluster Data Centre at CNES, Toulouse, where CESR-developed software will be running. Level-1 and Level-2 data products will thus be systematically generated. Level-1 files correspond to decommutated and decompressed data, organised in flat files, in full time resolution, one file per spacecraft-day-data product. Level-2 files are CDF files in physical units, and they include density for the major ion species, bulk velocity, parallel and perpendicular temperature. These files will be organised following the Cluster Science Data System (CSDS) recommendations, and they will populate two data bases: the Prime Parameter Data Base (PPDB: 4 spacecraft, 4 s resolution) and the Summary Parameter Data Base (SPDB: 1 spacecraft, 1 min resolution). The contents of these data bases will be distributed to other National Data Centres on a daily basis. The PPDB will be accessible to the whole Cluster community, and the SPDB will be public domain. Due to their broad accessibility, and to the quality of their data products, these data bases will permit joint analysis of plasma parameters from several instruments, further enhancing the science return of the Cluster mission.

The health and the performance of the CIS instrument will be monitored at various levels, by using files retrieved via the network from the Cluster Data Disposition System (DDS) , both at JSOC and at CESR.

5. Conclusion

The general characteristics of the two CIS instruments, including scientific performances, weight and raw power, are summarised in Table I. Note that the entrance of each sensor is put about 10 cm outside the spacecraft platform in order to have an unobstructed field of view and to minimise the effect of the spacecraft potential on the trajectories of the detected low-energy particles. The two planes of view of CODIF and HIA are parallel and tangential to the spacecraft body. The free field of view of the two sensors is $15^\circ \times 360^\circ$ (Figure 22).

In summary, by their unique features, the CIS instruments will provide fast measurements of the major plasma ion species with greatly improved accuracy and resolution. The inherent flexibility of the instrument control will allow a permanent optimisation of the scientific operation according to the various situations encountered all along the Cluster mission. The extensive on-board data processing will not only improve the time resolution of the measurements and significantly reduce data ground-processing costs, but will also make the plasma fundamental parameters quickly and directly available in an usable form to other investigators.

Acknowledgements

The CIS instrument was supported by many institutions. At CESR financial support came from CNES grant No. 208. The contribution of MPE Garching was supported by the Bunderministerium für Forschung und Technologie, Germany, under grant number 50 OC 89069. The high voltage supply of CIS-2 was provided by MPAE Lindau with the support of the Max-Planck-Gesellschaft zur Förderung der Wissenschaften and DARA grant 50 OC 89030. For IFSI CIS experiment was supported by Italian Space Agency (ASI). The work at the University of Washington, UNH, LPARL and UC Berkeley was supported by NASA contract. The Swedish participation was funded by the Swedish National Space Board and the Swiss participation by the Swiss National Science Foundation and the State of Bern.

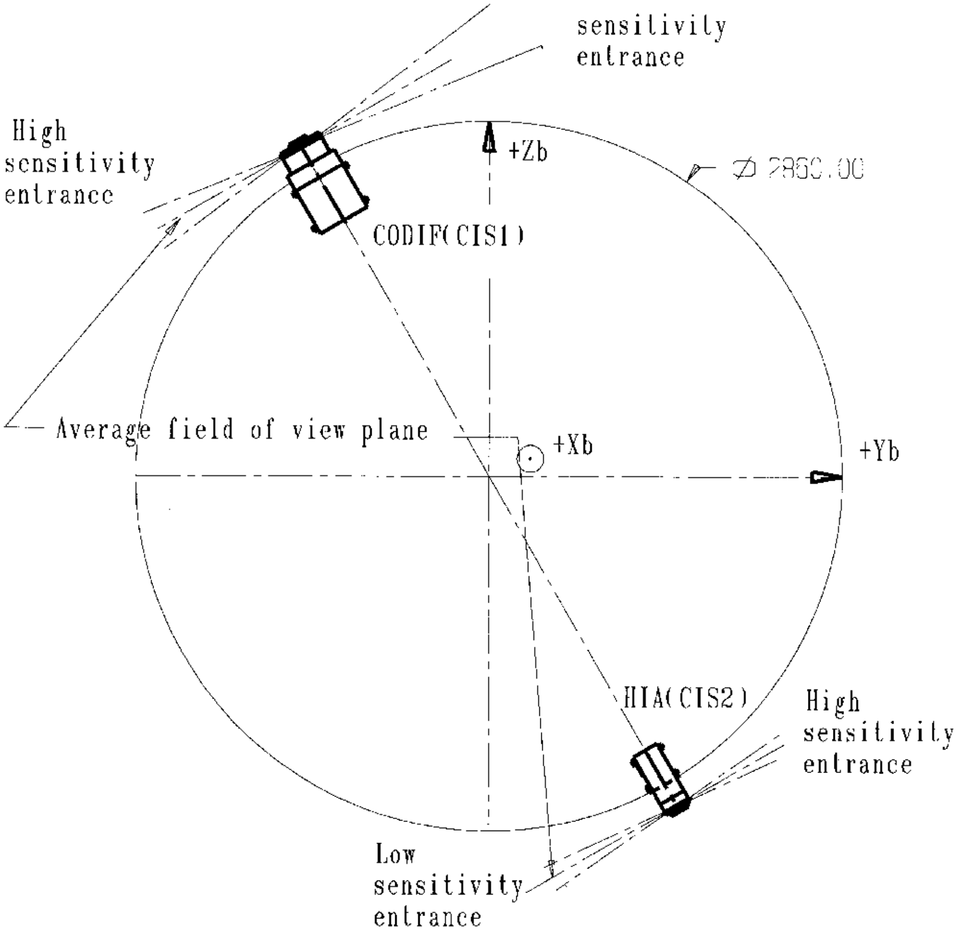

Figure 22. Position of the two sensors on the spacecraft and their fields of view.

We would like to thank J. P. Thouvenin for his permanent support and J. Y. Prado, H. Poussin, and M. Nonon-Latapie at CNES Toulouse, all the Cluster ESA Project staff at ESTEC and at ESOC for their excellent cooperation and the JSOC staff and particularly P. Chaizy in charge of the CIS instrument at JSOC.

The authors thank the 2 referees for their very efficient work.

References

Burgess, D.: 1989, ‘Cyclic Behaviour at Quasi-Parallel Collisionless Shocks’, *Geophys. Res. Letters* **16**, 345.

Carlson, C. W. *et al.*: 1982, ‘An Instrument for Rapidly Measuring Plasma Distribution Functions with High Resolution’, *Adv. Space Res.* **2** (7), 67.

Escoubet, P. C. and Schmidt, R.: 1997, ‘Cluster Science and Mission Overview’, *Space Sci. Rev.*, this issue.

Giacalone, J. *et al.*: 1994, 'Artificial Spacecraft in Hybrid Simulations of the Quasi-parallel Earth's Bow Shock: Analysis of Time Series Versus Spatial Profiles and a Separation Strategy for Cluster', *Ann. Geophys.* **12**, 591.

Gloeckler, G. *et al.*: 1993, 'Detection of Interstellar Pick-up Hydrogen in the Solar System', *Science* **261**, 70.

Lin, R. P. *et al.*: 1995, 'A Three-dimensional Plasma and Energetic Particle Investigation for the Wind Spacecraft', *Space Sci. Rev.* **71**, 125.

Martz, C.: 1993, 'Spectrométrie Ionique dans la Magnétosphère et le Vent Solaire. Simulation et Précision des Mesures Coordonnées au Moyen des 4 Satellites de la Mission Cluster', Thesis, Paul Sabatier Toulouse University.

Martz, C. and Sauvaud, J. A.: 1995, Accuracy of Ion Distribution Measurements and Related Parameters Using Top-hat Ion Spectrometers; Application to the CIS Cluster Experiment, submitted to *Rev. Sci. Instruments*.

Möbius, E. *et al.*: 1985, 'The Time-of-Flight Spectrometer SULEICA for Ions of the Energy Range 5-270 keV/charge on AMPTE IRM', *IEEE Trans. Geosc. Remote Sens.* **GE-23**, 274.

Möbius, E. *et al.*: 1985, 'Direct Observation of He^+ Pick-up Ions of Interstellar Origin in the Solar Wind', *Nature* **318**, 426.

Möbius, E. *et al.*: 1988, 'Interaction of Interstellar Pick-up Ions with the Solar Wind', *Astrophys. Space Sci.* **144**, 487.

Paschmann, G. *et al.*: 1985, 'The Plasma Instrument for AMPTE IRM', *IEEE Trans. Geosci. Remote Sens.* **GE-23**, 262.

Paschmann, G. *et al.*: 1986, 'The Magnetopause for Large Magnetic Shear: AMPTE/IRM Observations', *J. Geophys. Res.* **91**, 11099.

Quest, K. B.: 1988, 'Theory and Simulation of Collisionless Parallel Shocks', *J. Geophys. Res.* **93**, 9649.

Rème, H. *et al.*: 1987, 'The Giotto Electron Plasma Experiment', *J. Phys. E: Sci. Instrum.* **20**, 721.

Ritter, H.: 1985, 'Sekundärelektronenemission von Kohlenstoffolien beim Durchgang von Ionen im Energiebereich von 40 bis 500 keV', MPE Report 190.

Scholer, M.: 'Interaction of Upstream Diffuse Ions with the Solar Wind', *Adv. Space Sci.*, in press.

Scholer, M. and Terasawa, T.: 1990, 'Ion Reflection and Dissipation at Quasi-parallel Collisionless Shocks', *Geophys. Res. Letters* **17**, 119.

Sckopke, N. *et al.*: 1990, 'Ion Thermalization in Quasi-perpendicular Shocks Involving Reflected Ions', *J. Geophys. Res.* **95**, 6337.

Trattner, K. *et al.*: 1994, 'Statistical Analysis of Diffuse Ion Events Upstream at the Earth's Bow Shock', *J. Geophys. Res.* **99**, 13389.

Young, D. *et al.*: 1988, '2π-radian Field-of-View Toroidal Electrostatic Analyzer', *Rev. Sci. Instr.* **59**, 743.